THE ASTROPHYSICAL JOURNAL, 428:65–81, 1994 June 10

OBSCURATION, ORIENTATION, AND THE INFRARED PROPERTIES OF RADIO-LOUD ACTIVE GALAXIES

TIMOTHY M. HECKMAN,[1,2] CHRISTOPHER P. O'DEA,[2] STEFI A. BAUM,[2] AND EIJA LAURIKAINEN[3]
Received 1993 September 16; accepted 1993 December 10

ABSTRACT

We report on a study of the mid- and far-infrared (MFIR) properties of several different classes of radio-loud active galactic nuclei (AGNs) using the *IRAS* database. Our goal is to try to improve the understanding of the possible relationships between the diverse classes of AGNs. The MFIR and radio properties of radio-loud AGNs are especially useful in this regard, since (excluding the blazar class, which we do not study here) the radio emission is thought to be emitted isotropically, and the radio and MFIR radiation should be much less affected by dust obscuration than radiation at shorter wavelengths. We have first compared samples of 3CR broad-line radio galaxies (BLRGs) and narrow-line radio galaxies (NLRGs) matched in radio flux and mean redshift. We find that the BLRGs are stronger than the NLRGs by a factor of 4–5 in their mid-IR emission but are similar to the NLRGs in the far-IR. This is qualitatively consistent with recent "unification" models for NLRGs and BLRGs which invoke thermal MFIR emission from dusty "obscuring tori," but there may be an additional source of far-IR emission present in the more luminous broad-line objects (the radio-loud quasars) studied previously by Heckman, Chambers, & Postman (1992). We have also compared samples of Fanaroff-Riley class I (FRI) and Fanaroff-Riley class II (FRII) radio galaxies matched in radio flux and redshift. The FRII galaxies are stronger MFIR emitters than the FRI galaxies by a factor of about 4. This is consistent with suggestions that the central engine in FRI galaxies produces relatively little radiant energy per unit jet power (especially since we find that the weak MFIR emission from the FRI galaxies may not be powered by the AGN). Comparing samples of gigahertz-peaked spectrum (GPS) and compact steep spectrum (CSS) sources versus non–GPS-CSS sources, we find that the GPS-CSS and non–GPS-CSS sources have similar MFIR strengths. This suggests that the efficiency of the conversion of jet kinetic energy into radio emission is not much higher in the GPS-CSS sources, contrary to some theoretical predictions. Overall, we find that the MFIR and radio powers of all the classes of radio-loud AGNs we have studied correlate well with one another over a range of about 10^3 in power. This is most naturally understood if the MFIR is primarily powered by the AGN in most highly luminous radio-loud AGNs. However, other processes (starbursts or the intracluster medium) may contribute significantly in the less radio-luminous radio galaxies.

Subject headings: galaxies: active — galaxies: nuclei — infrared: galaxies — quasars: general

1. INTRODUCTION

Progress in understanding the fundamental physics that underlies the active galactic nucleus (AGN) phenomenon would surely be accelerated if the bewildering variety of AGNs could be attributed to well-understood secondary processes that modify the output of a single kind of AGN "central engine" (e.g., Blandford 1991). Borrowing from the lexicon of high-energy physics, the goal is a grand unified theory of AGNs. There has been considerable progress toward this goal, and it now seems clear that many of the observable properties of AGNs are determined in part by orientation and obscuration effects (e.g., Antonucci 1993; Lawrence 1991; Urry, Maraschi, & Phinney 1991). The central engines in AGNs emit at least some of their radiation anisotropically, and this anisotropy may be either intrinsic (e.g., relativistic beaming or radiation from an optically thick accretion disk) or induced (e.g., the escape of AGN light along the poles of a molecular torus or between the cracks of a swarm of molecular clouds). More broadly, it seems clear that many (but not all) of the observed differences between AGN classes may be the result of the luminous and mechanical output of one type of central engine interacting with systematically different types of circumnuclear environments.

This suggests that attempts to understand the relationships between different AGN classes should concentrate (at least initially) on the types of electromagnetic radiation that are the most likely to be emitted isotropically and the least likely to be affected by obscuration. A comparison of the mid- and far-infrared (MFIR) and radio properties of different classes of radio-loud AGNs is therefore particularly appropriate. Excluding the radio core–dominated subclass (where relativistic beaming is thought to be crucial), the low-frequency radio emission from radio-loud AGNs (which originates mostly from the large-scale radio lobes) is believed to be radiated nearly isotropically. Similarly, the MFIR emission from most AGN classes is now believed to be thermal emission from dust which has been heated by the central UV and optical radiation source. The small opacities of gas and dust in the MFIR mean that it will be relatively difficult to anisotropize such emission at a significant level. In fact, the most recent detailed models for the infrared emission from AGNs (Pier & Krolik 1992, 1993, hereafter PK92, PK93) predict that the

[1] Department of Physics & Astronomy, Johns Hopkins University, Baltimore, MD 21218.
[2] Space Telescope Science Institute, 3700 San Martin Drive, Baltimore, MD 21218.
[3] Turku University Observatory, Tuorla, SF-21500, Piikkio, Finland.

optical depth of the central source will drop below unity somewhere in the MFIR spectral region.

In the present paper, we will therefore use the *IRAS* data base to explore the relationships between three pairs of radio-loud AGN subclasses. Our approach of comparing the MFIR properties of carefully selected samples of specific classes of radio-loud active galaxies is complementary to previous investigations of the MFIR properties of radio galaxies and radio-loud quasars (see Neugebauer et al. 1986; Golombek, Miley, & Neugebauer 1988, hereafter GMN; Yates & Longair 1989; Knapp, Bies, & van Gorkom 1990; Impey, Wynn-Williams, & Becklin 1990; Impey & Gregorini 1993). We are primarily interested in determining the relationships between the above classes, rather than addressing the more general issues considered in the other studies. The three comparisons we will make are as follows.

1.1. *The Broad-Line Radio Galaxies and Narrow-Line Radio Galaxies*

It has been recently suggested that radio-loud quasars (RLQs) and their low-redshift counterparts, the broad-line radio galaxies (BLRGs), can be unified with narrow-line radio galaxies (NLRGs). The RLQs/BLRGs and the NLRGs are hypothesized to be drawn from the same parent population, but the BLRGs/RLQs are viewed more nearly parallel to the polar axis of a central dusty torus (which in turn aligns with the radio jet axis), while the NLRGs are viewed more nearly in the equatorial plane of the torus (Barthel 1989; Antonucci & Barvainis 1990). The optimal strategy for testing this hypothesis is to select samples of these classes on the basis of radiation that is almost surely emitted isotropically and then to compare the two classes using some different type of radiation that is also probably emitted isotropically (we thank S. Antonucci for repeating this argument to us on many occassions at diverse locations around the globe).

In an earlier paper (Heckman, Chambers, & Postman 1992, hereafter HCP), we made such a test using *IRAS* MFIR data for high-redshift ($z > 0.3$), high-luminosity samples of RLQs and NLRGs drawn from the 3CR sample. We concluded that the MFIR emission (at typically 6 to 60 μm in the AGN rest frame) is about three times stronger on-average in the RLQs than in NLRGs with the same mean redshift and low-frequency radio flux. We concluded that at least one of the following two statements must be true: 1) the RLQs are intrinsically stronger sources of MFIR emission than the NLRGs; 2) the MFIR radiation from RLQs and NLRGs is not emitted isotropically. If the first statement is true, then the simple unification scheme must be incorrect or incomplete. If the second statement is true, then the MFIR emission must be radiated anisotropically. Thus, the popular model (Sanders et al. 1989; PK92, PK93), in which the MFIR is thermal emission from dust, requires that the radiation source is both highly nonspherical and is also optically thick at wavelengths below about 60 μm. Alternatively, there may be a beamed nonthermal (blazar) contribution to the MFIR emission.

In the present paper we present a similar comparison but focus on a low-redshift sample (3CR radio galaxies with $z = 0.05$ to 0.30). This allows us to compare the MFIR properties of radio-loud objects with and without a broad-line region at longer rest wavelengths than was possible in HCP. This is important, because a thermal IR source will become increasingly optically thin (and will hence radiate more nearly isotropically) at longer IR wavelengths (PK92, PK93). It also allows us to study the MFIR properties of less powerful AGNs.

1.2. *The Fanaroff-Riley Class I and Class II Radio Galaxies*

Another long-standing puzzle concerns the relationship between the two morphologically distinct classes of large-scale radio sources associated with AGNs: the Fanaroff & Riley (1974) class I (FRI) sources, in which the radio surface brightness gradually decreases with increasing distance from the active nucleus, and the Fanaroff & Riley class II (FRII) sources, in which the highest surface brightnesses are typically found in the "hotspots" at the outer edges of the double radio lobes. The FRI's dominate the radio source population at intermediate levels of radio power ($L \approx 10^{40}$ to 10^{42} ergs s^{-1} between 10 MHz and 100 GHz), while the FRII's dominate at the higher power levels (see Miley 1980; Bridle & Perley 1984; Kellermann & Owen 1988 and references therein).

The lack of strong optical manifestations of nuclear activity in FRIs (see Hine & Longair 1979) has led to the idea that FRI's may have a qualitatively different sort of central engine than other types of AGNs—one that directs most of its output into the jet and produces relatively little optical and UV radiation (see Rees et al. 1982). However, it has never been quantitatively established that the ratio of AGN radiant luminosity to radio power is in fact anomalously low in FRI's: because the radio power of most FRI's is modest, it is to be expected that it will be more difficult to detect the weak optical signs of nuclear activity in these galaxies (see Morganti, Ulrich, & Tadhunter 1992). For most well-studied AGN classes, the MFIR is one of the most energetically important spectral regions (e.g., Sanders et al. 1989; Soifer, Houck, & Neugebauer 1987). It is therefore of interest to compare the MFIR properties of FRI and FRII radio galaxies within the range of radio luminosity where the two classes overlap (between about 10^{41} and 10^{43} ergs s^{-1}).

1.3. *The Gigahertz-peaked Spectrum and Compact Steep Spectrum Sources*

The gigahertz-peaked spectrum (GPS) and compact steep spectrum (CSS) sources are powerful but physically small (less than galaxy-scale) sources with turnovers in their radio spectra. The GPS sources have sub-kiloparsec sizes and spectral turnovers at frequencies of order 1 GHz. The CSS sources have sizes of 1–10 kpc and spectral turnovers at frequencies of 1 to several hundred MHz. They comprise approximately 5%–10% (GPS) and 20% (CSS) of radio-selected AGN samples and are thought to be isotropically emitting radio sources whose small size reflects their confinement by exceptionally dense circumnuclear gas (see Fanti et al. 1990a, b; O'Dea, Baum, & Stangellini 1991). This ambient medium might absorb and reprocess an unusually high fraction of the optical and UV output of the AGN in GPS or CSS sources, making them abnormally strong MFIR sources. However, it has also been suggested (e.g., Gopal-Krishna & Wiita 1991; De Young 1993) that jets which propogate through a medium of high density will convert jet mechanical energy into radio synchrotron emission with unusually high efficiency. In this case, a GPS or CSS source of a given radio power will be an intrinsically less luminous AGN than would another equally radio powerful non–GPS-CSS AGN. This argument might then suggest that the GPS and CSS sources would be deficient in their MFIR emission. The availibility of the *IRAS* database and new large samples of GPS and CSS sources allows us to test both these ideas.

2. SAMPLE SELECTION

2.1. *General Remarks*

All of the members of each of the samples we have investigated meet the following two criteria.

1. $|$*Galactic latitude*$| \geq 20°$.—This was adopted to minimize the effects of Galactic MFIR emission and thereby to maximize the sensitivity to the AGN MFIR emission.

2. *Observed in the "All Sky" Survey by IRAS.*—The "all sky" survey by *IRAS* covered only 96% of the sky. One member of our original FRII sample (1141+37) and two members of our original FRI sample (1144+25 and 1116+28) were not observed by *IRAS*.

2.2. *NLRG and BLRG Samples*

Our NLRG and BLRG samples are subsets of the revised 3C sample (3CR), originally chosen to be sources north of $\delta = -5°$ and brighter than 9 Jy at 178 MHz (Bennett 1962). We have selected our radio galaxies from the list of 3CR identifications compiled by Spinrad et al. (1985) and H. Spinrad (1993, private communication). Specifically, our final samples consist of the 45 NLRGs and the nine BLRGs in the 3CR sample (see Table 1) meeting the following additional criteria.

1. *Redshift in the range 0.05 to 0.3.*—The lowest redshift BLRG in the 3CR is 3C 390.3 at $z = 0.0561$, so this lower limit was adopted to insure a similar distribution in redshift for the BLRGs and NLRGs. HCP have already analyzed the corresponding samples at $z > 0.3$.

2. *Low-frequency radio emission is "lobe dominated."*—To insure that the BLRG and NLRG samples were selected on the basis of the strength of their ostensibly isotropic radio lobe emission, we have inspected the radio spectra of our sample (Kuhr et al. 1979). In only two cases (the well-known quasar 3CR 273 and the BL Lac object 3CR 371), that were subsequently excluded from our sample, did the radio spectrum have a complex form indicating that emission from an ultracompact synchrotron self-absorbed radio core (the putative Doppler-boosted relativistic jet) made a detectable contribution to the integrated radio emission at the frequency at which the sample was selected (178 MHz). This point is addressed more quantitatively in Table 2, where it can be seen that the mean radio spectral indices of the NLRG and BLRG samples are similar and are "normal" for lobe-dominated radio sources ($\langle\alpha\rangle = 0.7$ to 1.0 between 178 MHz and 14.9 GHz).

We have made the classification of NLRG or BLRG based on either published (e.g., Grandi & Osterbrock 1978; Miller 1981) or unpublished optical spectra (R. Laing, 1993 private communication). Our criterion for classifying a galaxy as a BLRG is the clear presence of a broad-line region (BLR) in the total flux spectrum. In some BLRGs, the BLR component can be seen only in Hα (but not in the higher members of the Balmer series). It is therefore possible that some of the NLRGs in our sample with the highest redshifts (and for which spectra of Hα are not available) may be misclassified BLRGs. Another complication is exemplified by 3CR 234, where spectropolarimetric data show that the BLR component is strongly polarized, suggesting that the BLR is seen only in reflection (Antonucci & Barvainis 1990). It is not clear whether to count this as a BLRG (since the BLR can be clearly discerned in the total flux spectrum) or as an NLRG (since the BLR may be seen only in reflection). In the absence of a uniform set of spectropolarimetric data, we have chosen the former option. We emphasize that none of the results disussed later in this paper depend critically on the classification of this (or any other) individual galaxy.

We note further that the semiquantitative spectroscopic classifications of the NLRGs given in Spinrad et al. (1985) imply that at least 70% of our NLRG sample have "strong emission-line" optical spectra. These galaxies generally have strong high-ionization emission lines and are spectroscopically similar to type 2 Seyfert galaxies (see Grandi & Osterbrock 1978; Koski 1978; Baum, Heckman, & van Breugel 1992). Only about 20% of the NLRGs in our sample are classified by Spinrad et al. as having "weak emission-line" or "absorption-line" optical spectra. These galaxies generally have low-ionization emission-line spectra of the low-ionization nuclear emission-line (LINER) variety (see Baum et al. 1992).

The samples of 3CR NLRGs and BLRGs are listed in Table 1, together with their most salient properties. A summary of the overall statistical properties of the subsamples is given in Table 2. The two are generally well matched in their distributions of redshift and radio flux density and are therefore also well matched in radio power (see Table 2 for details).

2.3. *FRI and FRII Samples*

The FRI and FRII samples were compiled from the following references: Laing, Riley, & Longair (1983, hereafter LRL); Owen & Laing (1989, hereafter OL); Fanti et al. (1987); and Caganoff (1989). The LRL list is a complete sample based on the 4C, 4CT, and 3CR catalogs and includes objects brighter than 10 Jy at 178 MHz and $\delta > +10°$. The OL list includes both 3CR and weaker sources. It is not a complete sample but was constructed to be representative of radio galaxies of low to medium redshift and radio power (see OL for details). The Fanti et al. set of radio galaxies is drawn from the Second Bologna (B2) Catalog and consists of two complete samples of B2 radio sources identified with galaxies down to two different limiting optical magnitudes (see Fanti et al. 1987 for details). The Caganoff sample is based on the Parkes 2.7 GHz southern sky survey and consists of all the Parkes radio sources satisfying the folowing criteria: 1) $\delta = -10°$ to $-35°$, 2) Flux density at 2.7 GHz ≥ 0.5 Jy, 3) identified with a galaxy having $m_B = 14$–18.

The FR classifications were generally taken from the above references. Fanti et al. did not give classifications, so we classified their sources by applying the Fanaroff & Riley (1974) morphological criteria to the best available radio maps. Radio sources with intermediate morphologies, including members of the "fat double" class (see OL) were excluded from all samples. This compilation resulted in samples of 75 FRI and 164 FRII sources, with the FRII's having substantially higher typical redshifts and radio powers. We therefore attempted to construct subsets of these two samples that provided a good match in redshifts and radio power between the two classes, while simultaneously including as many radio galaxies as possible. Our final matched samples observed by *IRAS* consist of 40 FRI and 28 FRII sources (see Tables 1 and 2).

2.4. *GPS-CSS and Comparison Samples*

Our samples of GPS and CSS sources were drawn primarily from two well-defined samples, with a few additional objects taken from the sample of O'Dea et al. (1991). The CSS sample defined by Fanti et al. (1990a) consists of those objects from the 3CR and Peacock & Wall (1982) catalogs satisfying the following criteria: 1) flux density at 178 MHz > 10 Jy, extrapolated from higher frequencies if necessary for sources with spectral

TABLE 1

THE SAMPLES

Object (1)	z (2)	$Flux_5$ (3)	P_5 (4)	$\alpha_{0.17-1.4}$ (5)	$\alpha_{1.4-5}$ (6)	$\alpha_{5-14.9}$ (7)
RG:[a]						
3C 13.0	1.351	0.400	27.52	0.92	1.22	1.17
3C 16.0	0.405	0.448*	26.29	0.88	1.10	0.00
3C 19.0	0.482	1.250	26.91	0.69	0.74	1.16
3C 34.0	0.689	0.299*	26.66	0.92	1.40	...
3C 41.0	0.794	1.450	27.49	0.57	0.72	0.95
3C 42.0	0.395	0.830	26.53	0.71	0.94	0.81
3C 44.0	0.660	0.280*	26.58	0.84	...	...
3C 46.0	0.437	0.266	26.14	0.97	1.30	...
3C 124.0	1.083	0.367*	27.23	...	...	...
3C 184.0	0.994	0.600	27.35	0.77	1.15	1.26
3C 200.0	0.458	0.660	26.58	0.96	0.91	...
3C 208.1	1.020	0.750	27.48	0.81	0.85	...
3C 210.0	1.169	0.490	27.45	0.86	1.00	1.36
3C 217.0	0.898	0.490	27.15	0.93	1.20	1.28
3C 220.3	0.680	0.600	26.95	0.85	1.26	...
3C 222.0	1.339	0.114*	26.97	...	...	...
3C 225.OA	0.134	0.271*	25.02	...	...	...
3C 225.OB	0.580	1.250	27.10	0.76	1.10	1.17
3C 226.0	0.817	0.509*	27.07	0.84	1.30	...
3C 228.0	0.552	1.130	27.00	0.76	0.92	1.04
3C 244.1	0.428	1.110	26.74	0.84	0.99	1.13
3C 247.0	0.749	0.940	27.24	0.78	0.91	1.21
3C 252.0	1.100	0.218*	27.03	1.04	1.40	...
3C 255.0	1.355	0.445*	27.57	...	...	...
3C 263.1	0.824	0.800	27.27	0.91	1.06	1.17
3C 266.0	1.275	0.534*	27.58	...	...	...
3C 267.0	1.140	0.650	27.54	0.87	1.03	0.95
3C 268.1	0.970	2.600	27.96	0.56	0.78	0.92
3C 268.2	0.362	0.380	26.11	0.94	1.08	0.58
3C 274.1	0.422	0.750	26.55	0.82	1.12	0.78
3C 275.0	0.480	0.970	26.80	0.72	1.01	0.57
3C 277.2	0.766	0.556*	27.04	0.93	0.90	...
3C 280.0	0.996	1.520	27.76	0.79	0.95	0.98
3C 289.0	0.967	0.600	27.32	0.82	1.11	1.09
3C 292.0	0.710	0.730	27.08	0.74	0.93	0.75
3C 295.0	0.461	6.500	27.58	0.62	0.96	1.28
3C 300.1	1.159	1.095*	27.78	0.75	0.80	...
3C 306.1	0.441	0.676*	26.55	0.96	0.80	...
3C 313.0	0.461	1.200	26.85	0.96	0.89	...
3C 320.0	0.342	0.500	26.17	0.82	1.01	1.16
3C 324.0	1.206	0.610	27.58	0.84	1.14	1.34
3C 325.0	0.860	0.820	27.33	0.71	1.19	1.08
3C 327.1	0.463	1.100	26.81	0.85	1.04	1.07
3C 330.0	0.550	2.330	27.31	0.61	0.89	1.19
3C 337.0	0.635	0.900	27.05	0.63	1.02	0.94
3C 340.0	0.775	0.750	27.18	0.78	0.91	1.04
3C 341.0	0.448	0.482*	26.42	0.89	1.18	...
3C 352.0	0.806	0.470	27.02	0.92	1.14	1.04
3C 356.0	1.079	0.380	27.25	1.12	1.05	1.21
3C 435.0	0.471	0.600	26.57	0.90	1.02	1.05
3C 441.0	0.707	0.910	27.17	0.81	0.83	1.12
GPSRG:[a]						
3C 49.0	0.621	0.900	27.03	0.66	0.89	1.03
3C 99.0	0.426	0.590*	26.46	0.92	0.80	...
3C 237.0	0.877	2.000	27.74	0.65	0.93	1.16
3C 241.0	1.617	0.410*	27.74	0.94	1.10	...
3C 299.0	0.367	0.900	26.50	0.75	0.92	1.13
3C 305.1	1.132	0.460	27.38	0.96	1.07	1.39
3C 318.0	0.752	0.750	27.15	0.81	1.01	1.08
3C 343.1	0.750	1.200	27.35	0.52	1.00	1.10
3C 434.0	0.322	0.390	26.00	0.96	0.88	0.70
0019−000	0.810**	1.070	27.38	...	...	0.84
0026+346	0.400**	1.575	26.82	...	...	0.88
0108+388	0.669	1.080	27.26	...	...	0.77
0316+161	1.170**	2.900	28.22	...	...	1.18
0320+053	0.575	0.900	26.95	...	...	1.33
0602+780	1.100**	0.180	27.44	...	...	...
0710+439	0.518	1.600	27.09	...	...	0.89
0752+342	1.050**	0.040	26.24	...	...	...
0914+114	0.430**	0.130	25.81	...	...	1.08
0941−080	0.300**	1.130	26.40	...	...	1.07
1031+567	0.459	1.230	26.85	...	...	0.96
1323+321	0.369	2.310	26.91	...	...	0.77
1341+144	1.050**	0.400	27.24	...	...	1.37
1358+624	0.429	1.708	26.93	...	...	0.96
1518+047	1.296	1.000	27.86	...	1.09	2.02
1543+005	0.550	0.900	26.90	...	...	1.01
1604+315	1.500**	0.600	27.82	...	...	0.64
1732+094	0.550**	0.900	26.90	...	...	1.01
1751+278	0.860**	0.240	26.80	...	...	0.64
1819+39	0.400	0.990	26.62	...	...	1.34
2008−068	1.050**	1.350	27.77	...	...	0.74
2128+048	1.000**	2.009	27.88	...	...	0.88
2147+145	1.170**	0.700	27.60	...	...	1.30
2149+056	0.700**	1.040	27.21	...	...	0.50
QSR[a]						
3C 2.0	1.037	1.450	27.78	0.66	0.74	0.76
3C 9.0	2.012	0.550	28.12	1.04	1.05	1.31
3C 14.0	1.469	0.600	27.79	0.85	0.91	1.26
3C 47.0	0.425	1.200	26.77	0.98	0.91	1.09
3C 68.1	1.238	0.800	27.72	0.91	0.91	1.13
3C 93.0	0.358	0.900	26.47	0.83	0.91	1.09
3C 109.0	0.306	1.700	26.59	0.82	0.69	0.81
3C 191.0	1.956	0.528*	28.07	0.75	1.00	...
3C 196.0	0.871	4.300	28.06	0.85	0.93	1.14
3C 204.0	1.112	0.341*	27.23	0.98	1.10	...
3C 205.0	1.534	0.670	27.89	0.82	1.01	1.30
3C 207.0	0.684	1.400	27.32	0.76	0.53	0.60
3C 208.0	1.110	0.570	27.44	1.01	1.10	1.28
3C 212.0	1.049	0.860	27.57	0.84	0.90	0.53
3C 215.0	0.420	0.420	26.28	0.96	1.05	1.07
3C 220.2	1.157	0.590	27.51	0.79	0.88	0.82
3C 245.0	1.029	1.450	27.77	0.68	0.65	0.49
3C 249.1	0.311	0.770	26.27	0.80	0.91	0.83
3C 254.0	0.734	0.780	27.14	0.97	1.11	1.24
3C 263.0	0.656	1.030	27.14	0.76	0.87	1.36
3C 270.1	1.519	0.860	27.99	0.79	0.89	0.61
3C 275.1	0.557	0.900	26.91	0.84	0.93	0.50
3C 277.1	0.320	1.040	26.42	0.75	0.71	1.13
3C 288.1	0.961	0.400	27.14	0.94	1.04	1.26
3C 334.0	0.555	0.600	26.73	0.81	1.02	0.63
3C 336.0	0.927	0.730	27.36	0.79	1.03	1.13
3C 351.0	0.371	1.200	26.63	0.73	0.79	0.96
3C 432.0	1.805	0.363*	27.81	0.91	1.20	...
GPSQSR:[b]						
3C 43.0	1.470	1.100	28.06	0.71	0.76	0.81
3C 48.0P	0.367	5.300	27.27	0.61	0.86	1.02
3C 67.0P	0.310	0.900	26.33	...	0.64	1.00
3C 186.0P	1.063	0.380	27.23	1.15	1.00	...
3C 190.0P	1.197	0.850	27.71	0.88	0.89	0.95
3C 216.0P	0.670	1.800	27.41	0.84	0.61	0.32
3C 268.3P	0.371	1.100	26.59	...	0.54	1.09
3C 286.0	0.849	7.430	28.27	0.27	0.55	0.70
3C 287.0	1.055	3.200	28.15	0.44	0.32	0.74
3C 298.0	1.439	1.500	28.17	1.04	1.09	0.71
3C 309.1	0.904	3.700	28.04	0.52	0.65	0.82
3C 343.0P	0.988	1.500	27.74	0.50	0.91	1.32
3C 380.0	0.691	7.000	28.03	0.75	0.55	0.76
3C 454.0	1.757	0.750	28.10	0.80	0.85	0.83
3C 455.0P	0.543	0.850	26.86	0.70	0.98	1.27
0615+820P	0.710	1.053	26.94	...	1.39	...
0738+313P	0.630	2.000	27.39	...	...	0.71
1245−197	1.279	2.500	28.25	...	...	0.75
1153+31	1.557	0.950	28.06	...	...	1.30
1404+286	0.077	2.900	25.55	...	...	0.57
2137+209P	1.576	0.510	27.80	...	...	...
2230+114	1.037	3.600	28.18	...	...	0.42

TABLE 1—*Continued*

Object (1)	z (2)	$Flux_5$ (3)	P_5 (4)	$\alpha_{0.17-1.4}$ (5)	$\alpha_{1.4-5}$ (6)	$\alpha_{5-14.9}$ (7)
NLRG:[b]						
3C 15.0P	0.073	1.600	25.24	0.67	0.78	0.95
3C 17.0P	0.220	2.600	26.46	0.60	0.71	0.67
3C 18.0P	0.188	1.700	26.13	0.77	0.76	0.87
3C 33.0P	0.060	5.400	25.59	0.70	0.74	0.60
3C 55.0P	0.240	0.870	26.07	1.00	0.88	1.22
3C 61.1P	0.186	1.900	26.17	0.51	0.92	...
3C 63.0P	0.175	0.850	25.76	0.88	1.09	1.20
3C 79.0P	0.256	1.400	26.34	0.88	0.98	1.35
3C 89.0P	0.139	0.800	25.52	1.00	1.00	1.23
3C 105.0P	0.089	2.200	25.56	0.61	0.69	1.04
3C 135.0P	0.127	1.030	25.55	0.83	0.93	0.87
3C 171.0P	0.238	1.210	26.21	0.89	0.90	1.04
3C 173.1P	0.292	0.800	26.22	0.83	0.98	1.00
3C 184.1P	0.118	1.230	25.56	0.70	0.80	...
3C 192.0P	0.060	2.100	25.18	0.76	0.67	0.78
3C 197.1P	0.130	0.850	25.49	0.79	0.65	1.20
3C 198.0	0.082	0.504*	24.84	0.82	1.00	...
3C 213.1P	0.194	0.830	25.85	0.78	0.69	0.85
3C 219.0P	0.174	2.270	26.19	0.83	1.05	1.22
3C 223.0P	0.137	1.300	25.72	0.76	0.71	0.74
3C 223.1P	0.108	0.850	25.32	0.86	0.65	0.92
3C 236.0P	0.099	1.300	25.43	0.89	0.73	0.45
3C 258.0P	0.165	0.400	25.38	1.07	0.83	0.84
3C 277.3P	0.086	1.220	25.27	0.73	0.71	0.78
3C 284.0P	0.239	0.690	25.97	0.88	0.86	1.60
3C 285.0	0.079	0.750	24.99	0.85	0.85	1.21
3C 288.0P	0.246	0.980	26.15	0.85	1.00	1.29
3C 300.0P	0.270	1.100	26.28	0.77	0.95	1.16
3C 303.0P	0.141	0.930	25.60	0.80	0.78	0.39
3C 310.0	0.054	1.300	24.88	0.89	1.41	...
3C 314.1P	0.120	0.330	25.00	0.91	1.26	0.85
3C 315.0P	0.108	1.300	25.51	0.77	0.90	0.88
3C 319.0P	0.192	0.650	25.73	0.87	1.09	0.99
3C 321.0P	0.096	1.200	25.36	0.67	0.84	1.03
3C 326.0	0.090	0.450	24.87	0.81	0.36	...
3C 327.0P	0.104	3.200	25.86	0.73	0.82	0.90
3C 348.0P	0.154	12.500	26.81	1.04	1.02	1.25
3C 349.0P	0.205	1.130	26.04	0.71	0.83	0.82
3C 357.0P	0.166	1.000	25.79	0.66	0.78	0.99
3C 379.1P	0.256	0.650	26.01	0.81	0.76	1.63
3C 424.0P	0.222	0.650	25.35	0.88	1.06	1.13
3C 456.0P	0.233	0.700	25.95	0.80	1.03	0.98
3C 458.0P	0.290	0.950	26.29	0.78	0.85	1.06
3C 459.0P	0.220	1.360	26.18	0.97	0.90	1.10
3C 460.0P	0.268	0.291*	25.70	...	...	...
BLRG:[a]						
3C 67.0	0.310	0.900	26.33	0.64	0.95	1.01
3C 227.0	0.086	2.700	25.62	0.74	0.77	0.95
3C 234.0	0.185	1.530	26.07	0.89	0.99	1.02
3C 287.1	0.216	1.500	26.21	0.60	0.56	0.70
3C 323.1	0.264	0.910	26.18	0.72	0.79	0.85
3C 332.0	0.152	0.820	25.61	0.68	0.89	0.73
3C 381.0	0.161	1.280	25.86	0.70	0.88	0.81
3C 390.3	0.056	4.450	25.45	0.70	0.80	0.73
3C 445.0	0.056	2.100	25.13	0.74	0.78	0.88
FRI:[a]						
3C 28.0	0.195	0.412*	25.55	1.11	1.90	...
3C 218	0.065	14.0	26.08	0.92	...	...
3C 272.1	0.003	2.900	22.73	0.58	0.60	0.74
3C 315.0	0.108	1.300	25.51	0.77	0.90	0.88
0007+124	0.110	0.730*	25.27	0.78	0.79	...
0108−142	0.052	0.580	24.50	...	0.57	...
0115−261	0.053	0.330	24.28	...	0.89	...
0116−190	0.280	0.430	25.91	...	0.84	...
0149+35	0.016	0.054*	22.43	...	0.70	...
0222+36	0.033	0.111*	23.37	...	0.60	...
0229−208	0.090	0.470	24.90	...	0.76	...
0304−122	0.079	0.380	24.69	...	1.08	...
0434−225	0.069	0.390	24.58	...	0.86	...
0456−301	0.131	0.900	25.52	...	0.88	...
0533−120	0.157	0.640	25.54	...	0.67	...
0545−199	0.053	0.420	24.38	...	0.55	...
0836+29	0.079	0.409*	24.72	0.40	0.60	...
0838+32	0.068	0.304*	24.46	0.48	0.70	...
0843+31	0.067	0.019*	23.23	...	...	...
0922+36	0.113	0.235*	24.80	0.66	0.90	...
1005+28	0.148	0.035*	24.22	...	...	...
1053−282	0.061	0.890	24.83	...	0.59	...
1102+30	0.072	0.134*	24.15	...	1.70	...
1103−244	0.234	0.370	25.68	...	0.99	...
1108+27	0.033	0.032*	22.84	...	...	...
1116+28	0.067	0.164*	24.17	...	0.90	...
1144+35	0.063	0.695*	24.75	...	...	...
1227+119	0.100	0.617*	25.11	0.92	0.80	...
1243+26	0.089	0.163*	24.43	...	0.70	...
1258−229	0.130	0.390	25.15	...	0.70	...
1300+32	0.164	0.110*	24.82	...	0.80	...
1324−300	0.200	0.330	25.48	...	0.92	...
1357+28	0.063	0.116*	23.97	...	0.60	...
1521+28	0.083	0.352*	24.69	0.52	0.70	...
1528+29	0.084	0.051*	23.87	...	1.30	...
1621+38	0.031	0.172*	23.52	...	0.60	...
2013−308	0.089	0.280	24.66	...	0.94	...
2058−282	0.039	1.820	24.73	...	0.88	...
2058−135	0.046	0.520	24.34	...	0.72	...
2134−281	0.071	0.370	24.58	...	0.89	...
2225−308	0.055	0.340	24.31	...	0.78	...
FRII:[a]						
3C 16.0	0.405	0.470*	26.31	0.86	1.09	...
3C 35.0	0.067	0.590	24.73	0.85	1.02	...
3C 98.0	0.031	4.700	24.92	0.77	0.61	...
3C 285.0	0.079	0.750	24.98	0.85	0.85	1.21
3C 326.0	0.090	0.450	24.87	0.83	1.41	...
0120+33	0.016	0.059*	22.47	...	0.75	...
0247−207	0.087	0.300	24.67	...	0.95	...
0307−305	0.067	0.390	24.55	...	0.81	...
0326−288	0.108	0.540	25.12	...	0.70	...
0511−305	0.058	0.750	24.71	...	0.98	...
0548−317	0.033	0.430	23.97	...	0.75	...
0800+24	0.043	0.047*	23.24	...	1.10	...
0836+29A	0.065	0.267*	24.36	0.48	0.80	...
0844+31	0.068	0.563*	24.71	...	...	...
0828+32	0.051	0.450*	24.35	0.10	1.20	...
1017+487	0.053	0.089*	23.70	1.59	0.51	...
1141+37	0.115	0.421*	25.07	0.23	1.34	...
1205+341	0.078	0.220	24.44	...	0.60	...
1254−300	0.054	0.370	24.34	...	0.99	...
1323−271	0.043	0.500	24.27	...	1.02	...
1329−328	0.048	0.284	24.12	...	0.78	...
1423−177	0.107	0.400	24.98	...	0.91	...
1441+25	0.062	0.048*	23.57	...	1.20	...
1449−129	0.069	0.470	24.66	...	0.80	...
1455+287	0.141	0.302*	25.11	0.69	0.80	...
1615+32	0.152	0.887*	25.65	0.59	0.90	...
2053−201	0.156	0.990	25.72	...	0.76	...
2117−269	0.103	0.420	24.97	...	0.55	...
2236−176	0.074	0.540	24.78	...	0.80	...

NOTES.—Asterisk (*) denotes interpolated or extrapolated value; two asterisks (**) denote z estimated using the m-z diagram for 3C radiogalaxies. P after source name means that the object is a member of a power-selected sample.

[a] Redshift and power selected sample.

[b] Redshift selected sample.

TABLE 2

MEAN VALUES OF SAMPLE PARAMETERS

Sample (1)	log $P_{5\ GHz}$ (W/Hz^{-1}) (2)	Redshift (3)	$S_{5\ GHz}$ (Jy) (4)	Spectral Index (178–1400 MHz) (5)	Spectral Index (1.4–5 GHz) (6)	Spectral Index (5–14.9 GHz) (7)
RG (z, P)	27.0 (51)	0.753 (51)	0.875 (51)	0.825 (46)	1.027 (45)	1.057 (32)
GPSRG (z, P)	27.1 (33)	0.766 (33)	1.035 (33)	0.797 (9)	0.969 (10)	1.025 (29)
QSR (z, P)	27.3 (28)	0.945 (28)	0.964 (28)	0.844 (28)	0.919 (28)	0.973 (25)
GPSQSR (z)	27.6 (22)	0.934 (22)	2.289 (22)	0.708 (13)	0.786 (16)	0.847 (19)
GPSQSR (P)	27.2 (11)	0.766 (11)	1.386 (11)	0.780 (6)	0.869 (9)	0.960 (8)
NLRG (z)	25.7 (45)	0.162 (45)	1.496 (45)	0.809 (44)	0.867 (44)	1.00 (44)
NLRG (P)	25.8 (41)	0.170 (41)	1.569 (41)	0.805 (40)	0.864 (40)	0.99 (40)
BLRG (z, P)	25.8 (9)	0.165 (9)	1.799 (9)	0.7113 (9)	0.822 (9)	0.85 (9)
FRI (z, P)	24.6 (42)	0.090 (42)	0.826 (42)	...	0.829 (38)	...
FRII (z, P)	24.6 (29)	0.087 (29)	0.576 (29)	0.713 (11)	0.891 (28)	...

NOTES.—Col. (1): sample; the letter in parentheses designates the criteria for matching the sample, e.g., (z) means the sample was matched on redshift. Col. (2): power in watts per Hz at 5 GHz in the rest frame of the source. The number of objects used in calculating the mean value is given in parentheses. Col. (3): heliocentric optical redshift. The number of objects used in calculating the mean value is given in parentheses. Col. (4): flux density at 5 GHz. The number of objects used in calculating the mean value is given in parentheses. Col. (5): spectral index between 178 and 1400 MHz. The number of objects used in calculating the mean value is given in parentheses. Col. (6): spectral index between 1.4 and 5.0 GHz. The number of objects used in calculating the mean value is given in parentheses. Col. (7): spectral index between 5.0 and 14.9 GHz. The number of objects used in calculating the mean value is given in parentheses.

turnovers above 178 MHz; 2) monochromatic radio power at 178 MHz $> 10^{27}$ W Hz^{-1} for $H_0 = 75$ km s^{-1} Mpc^{-1} and $q_0 = 0$; 3) projected linear size <20 kpc; 4) |Galactic latitude| $> 10°$ and $\delta > 10°$.

The GPS sample defined by Stangellini et al. (1990) satisfies the folowing criteria: 1) flux density at 5 GHz > 1 Jy; 2) turnover frequency between 0.4 and 5 GHz; 3) spectral index steeper than 0.5 in the high-frequency portion of the radio spectrum (to exclude flat spectrum objects and blazars); 4) |Galactic latitude| $> 10°$ and $\delta > -25°$.

Since GPS-CSS and "normal" radio sources have such different radio spectral shapes, it is not clear a priori at which frequency one should attempt to match the fluxes between a GPS-CSS sample and a comparison sample. The spectral curvature at low frequencies in GPS-CSS sources is thought to arise owing to either optical depth effects in the synchrotron source or free-free absorption by foreground ionized gas. In either interpretation, it seems most straightforward to compare GPS-CSS and non–GPS-CSS samples which are matched in radio flux and power at high frequencies where the synchrotron source and/or the ionized foreground gas is optically thin in the GPS-CSS sources. We have therefore chosen 5 GHz as our reference frequency in our attempts to construct comparison samples.

Comparison samples of non–GPS-CSS radio galaxies and quasars that matched the corresponding GPS-CSS samples in mean redshift and radio power were constructed from the 3CR catalog (after excluding all the GPS and CSS sources and also those few sources with complex or inverted radio spectra—e.g., 3CR 273, 3CR 345, and 3CR 454.3). Our final comparison samples consist of 51 radio galaxies and 28 quasars. Our final GPS-CSS radio galaxy sample contains 33 objects. Because many of the known GPS quasars are exceptionally powerful objects at very high redshift (O'Dea 1990a, b; O'Dea et al. 1991), it proved difficult to construct a single pair of GPS-CSS and non–GPS-CSS quasar samples that were well matched in both redshift and radio power. We have therefore utilized two different GPS-CSS quasar samples: one optimally matched to the comparison sample in radio power (11 GPS-CSS quasars) and one optimally matched to the comparison sample in redshift (22 GPS-CSS quasars). The members of all these samples are listed in Table 1, and a comparison of the relevant statistics characterizing the samples is given in Table 2.

3. DATA ANALYSIS

IRAS surveyed 96% of the sky at four wavelength bands: 12, 25, 60, and 100 μm (Beichman et al. 1984). Typical limiting flux densities in the fully co-added *IRAS* "faint source" database for point sources (size < several arcmin) are approximately 80, 100, 100, and 400 mJy at these four respective wavebands. Previous investigations of the MFIR properties of radio galaxies and quasars using *IRAS* data have shown that such objects can be powerful sources of MFIR emission (Neugebauer et al. 1986; GMN; Yates & Longair 1989; Knapp et al. 1990; Impey et al. 1990; HCP; Impey & Gregorini 1993).

Quantitative comparisons of the MFIR properties of different classes of radio-loud AGNs have been difficult because of the limited sensitivity of *IRAS* in its all-sky survey mode and by the relatively few such objects targeted for the more sensitive pointed observations by *IRAS*. Deep, pointed observations with *IRAS* (typically with sensitivities about twice as good as the limits listed in the preceding paragraph) have been reported for a small fraction of the objects in our samples in Table 1 by GMN and Neugebauer et al. (1986), and only 12 of these objects have been detected. We have also inspected the co-added *IRAS* data for all the individual sources in all our samples. An additional 14 objects (other than those with deep pointed observations published in the above references) have been reliably detected ($>4\ \sigma$ detection in two or more *IRAS* bands). All 26 individual detections are given in Table 3.

The development of the SUPERSCANPI algorithm at IPAC now makes it possible to improve significantly upon the *IRAS* flux limits given above for an ensemble of a large number of targets. Given a target list, SUPERSCANPI co-adds all the survey data (scans) for all members of the sample to produce a signal for the entire ensemble of targets. The data may be combined in SUPERSCANPI in a variety of ways. Experiments show that the data are sufficiently well behaved that a Poissonian improvement in sensitivity by a factor $\sqrt{N}$ can nearly be achieved at 12, 25, and 60 μm for an ensemble of N

TABLE 3

INDIVIDUAL DETECTIONS

Object (1)	Sample (2)	12μ (3)	25μ (4)	60μ (5)	100μ (6)
3C 47	non-GPS Q	<96	<126	180 ± 40	440 ± 110
3C 48	GPS Q	56 ± 6	160 ± 8	770 ± 9	1080 ± 27
3C 79	NLRG	27 ± 7	62 ± 13	179 ± 9	<330
3C 109	non-GPS Q	67 ± 8	190 ± 16	248 ± 13	<227
3C 218	FRI	<30	<35	155	416
3C 234	BLRG	144 ± 13	355 ± 27	265 ± 17	<142
3C 249.1	non-GPS Q	17 ± 5	45 ± 6	61 ± 9	<85
3C 272.1	FRI	128 ± 37	<152	556 ± 51	1187 ± 126
3C 285	FRII, NLRG	<84	70 ± 14	290 ± 48	590 ± 144
3C 300	NLRG	<101	146 ± 38	191 ± 51	546 ± 105
3C 318	GPS G	<99	<78	170 ± 26	300 ± 70
3C 321	NLRG	<93	300 ± 34	1070 ± 31	1170 ± 48
3C 327	NLRG	110 ± 25	300 ± 24	640 ± 31	370 ± 93
3C 351	non-GPS Q	46 ± 5	125 ± 5	183 ± 9	<299
3C 381	BLRG	<37	74 ± 13	64 ± 21	<198
3C 390.3	BLRG	151 ± 7	368 ± 9	214 ± 13	302 ± 38
3C 445	BLRG	171	349	280	<450
3C 459	NLRG	<123	110 ± 31	650 ± 38	990 ± 107
0149+35	FRI	<30	<47	273 ± 17	1247 ± 56
0307−305	FRII	<57	160 ± 24	260 ± 36	<321
0326−288	FRII	<42	260 ± 25	500 ± 24	490 ± 126
0738+313	GPS Q	<20	<39	145 ± 9	<282
0836+299	FRII	<21	149 ± 18	487 ± 13	614 ± 38
1404+286	GPS Q	250 ± 30	400 ± 37	770 ± 30	960 ± 101
1441+262	FRII	<54	<57	170 ± 34	430 ± 103
1521+288	FRI	<66	<78	170 ± 26	300 ± 70

NOTES.—Col. (1): object. Col. (2): sample. GPS means GPS/CSS. Cols. (3)–(6): *IRAS* flux density in mJy taken from the deep pointed observations reported in Neugebauer et al 1986, GMN, or Impey & Gregorini (1993). When unavailable, we have used the *IRAS* co-additions from the present study. In these cases we have used the point-spread function (PSF) template-fitting algorithm and the median scan.

targets compared to an individual target. The situation at 100 μm is more complex because of the brightness of patchy Galactic cirrus emission.

Accordingly, we have separately processed each of the samples described above through SUPERSCANPI. For each of the four *IRAS* spectral bands, the SUPERSCANPI algorithm was first instructed to produce a one-dimensional map (surface brightness vs. sky position) for each individual target. These were constructed from the median of the multiple scans made by *IRAS* through that target. The median was used, as this is the most robust estimator for individual targets (since it rejects "glitches" in individual scans).

Next, these one-dimensional maps of all the targets in a given sample were combined in three ways: by computing the median, the straight mean, and the weighted mean of the set (where the weighting in this last quantity was by the inverse square of the noise in a map of a given target). These three estimators are complementary to one another: the median is the least sensitive to the effect of a handful of very bright sources in a sample, the straight mean is the most straightforward to interpret, and the weighted mean, in principle, provides the highest signal-to-noise ratio in the final map of the sample.

These final maps were then inspected for a signal. Since we expect the MFIR emission from our targets to be unresolved spatially by *IRAS* (the *IRAS* beam is of the order of several hundred kpc to a Mpc in projected size at these redshifts), we have determined the fluxes of the detections by fitting a template of the *IRAS* point-spread-function at the appropriate wavelength to the data. Uncertainties in these fitted fluxes are taken to be the rms noise in the map, and upper limits for nondetections were set at 3 times the rms noise.

4. RESULTS

4.1. *BLRGs versus NLRGs*

The outcome of our SUPERSCANPI analysis of the BLRG and NLRG 3CR samples is given in Tables 4 and 5. The primary result is that the ratio of BLRG to NLRG flux (expressed either as a ratio of means or a ratio of medians) increases monotonically with decreasing wavelength. While the ratio is about four or five at 12 μm, it decreases to near unity at 100 μm. This is shown graphically in Figure 1, which is a plot of the mean (Fig. 1*a*), median (Fig. 1*b*), and weighted mean fluxes (Fig. 1*c*) as a function of mean rest wavelength.

HCP conducted a similar analysis of samples of 3CR radio galaxies and quasars at $z > 0.3$ and found that the quasars were consistently brighter by factors ranging from about 2 to 6 in all the *IRAS* bands. In comparing the HCP results to those presented here, it is important to consider, however, that there are systematic differences in the range of rest wavelengths probed by the *IRAS* data for the high-redshift (HCP) and low-redshift (the present paper) samples. Since $\langle z \rangle = 0.16$ for the present sample, these new *IRAS* data probe the wavelength range from about 10 to 86 μm in the AGN rest frame. The mean redshift was $\langle z \rangle = 0.94$ for the entire HCP sample, so that those *IRAS* data instead typically sampled the wavelength range between 6 and 52 μm in the AGN rest frame. The HCP results are compared graphically to the present results in Figure 2. Note the clear wavelength dependence of the flux

TABLE 4

SUMMARY OF MEAN *IRAS* PROPERTIES

	12μ			25μ			60μ			100μ		
SAMPLE (1)	Mean (2)	Median (3)	Weighted Mean (4)	Mean (5)	Median (6)	Weighted Mean (7)	Mean (8)	Median (9)	Weighted Mean (10)	Mean (11)	Median (12)	Weighted Mean (13)
RG (z, P)	<9	<9	<9	<15	16 ± 4	<9	18 ± 5	25 ± 5	<12	45 ± 9	51 ± 10	<39
GPSRG (z, P)	<15	<12	<12	<15	<15	<12	30 ± 8	<27	27 ± 7	<126	<102	<69
QSR (z, P)	<15	18 ± 4	19 ± 5	40 ± 6	29 ± 4	54 ± 4	62 ± 6	51 ± 5	68 ± 5	191 ± 43	114 ± 29	<100
GPSQSR (z)	<15	<12	<9	29 ± 7	21 ± 7	31 ± 4	100 ± 8	39 ± 8	102 ± 8	95 ± 21	92 ± 24	113 ± 29
GPSQSR (P)	<24	<24	20 ± 6	25 ± 8	<21	28 ± 7	112 ± 11	51 ± 11	109 ± 8	163 ± 38	227 ± 34	140 ± 48
NLRG (z)	13 ± 4	14 ± 4	15 ± 4	22 ± 4	12 ± 3	25 ± 4	76 ± 6	31 ± 5	84 ± 6	212 ± 27	122 ± 22	209 ± 21
NLRG (P)	<15	14 ± 4	15 ± 4	21 ± 4	13 ± 3	25 ± 4	74 ± 7	28 ± 5	84 ± 6	210 ± 30	111 ± 24	209 ± 23
BLRG (z, P)	86 ± 12	63 ± 11	81 ± 11	109 ± 12	60 ± 7	107 ± 8	111 ± 12	77 ± 12	103 ± 11	171 ± 64	188 ± 56	132 ± 31
FRI (z, P)	16 ± 3	13 ± 4	14 ± 4	<15	<15	30 ± 5	24 ± 8	18 ± 6	32 ± 8	66 ± 20	<63	139 ± 21
FRII (z, P)	<15	12 ± 4	<15	30 ± 5	16 ± 5	37 ± 5	86 ± 7	61 ± 6	112 ± 6	130 ± 12	171 ± 17	148 ± 15

NOTES.—Col. (1): sample under consideration. The letter in parentheses designates the criteria for matching the sample, e.g., (z) means the sample was matched on redshift. Cols. (2)–(13): mean value of flux density or 3 σ upper limit (in mJy) derived from the SUPERSCANPI output via *IRAS* PSF template fitting. The mean is a straight mean which weights all the targets equally, and the weighted mean weights the target fields by the inverse square of the rms noise in a target field. We also give the median which is least sensitive to the effect of a few bright sources.

ratio for the present low-redshift sample, the lack of any strong wavelength dependence of the flux ratio for the HCP high-redshift sample, and the extension to longer rest wavelengths provided by the present sample.

HCP also analysed a lower redshift subset of their entire sample with $\langle z \rangle = 0.54$, which then samples the average wavelength range from about 8 to 65 μm. To investigate any possible redshift and/or luminosity dependence of the MFIR properties, we have also examined the ratios of the MFIR fluxes in the $\langle z \rangle = 0.54$ subset of the HCP sample. The results of this examination are also displayed in Figure 2 and are consistent with the results for the full HCP sample.

The behavior of the ratios of both the straight and weighted mean fluxes as a function of rest wavelength (see Table 5 and Figs. 1 and 2) implies that there is an intrinsic luminosity (or redshift) dependence of the MFIR properties of radio-loud AGNs. Only the wavelength dependence of the ratios of the median fluxes suggests that the HCP and new results are consistent with one another, with flux ratio being a simple inverse function of MFIR rest wavelength. We note in passing that the clear MFIR wavelength dependence of the MFIR/radio ratio seen in the BLRG versus the NLRG samples is also seen in radio-quiet AGNs (Seyfert galaxies). Ulvestad (1986) found that the mean ratio of mid-IR (10 μm) to radio flux is a factor of at least 3 larger for type 1 Seyferts than for type 2 Seyferts. In contrast, Dahari & DeRobertis (1988) found that the mean ratio of far-IR (60 μm) to radio flux is only a factor of $\approx$1.3 greater for the type 1 Seyferts.

We have computed "characteristic luminosities" at a rest wavelength of $\approx$50 μm for the NLRG and BLRG samples

TABLE 5

MFIR FLUX DENSITY RATIOS NORMALIZED BY MEAN RADIO FLUX DENSITIES

Sample (1)	Type (2)	12μ (3)	25μ (4)	60μ (5)	100μ (6)
GPSRG (z, P)/RG (z, P)	Straight	...	...	1.41 ± 0.64	<2.4
GPSRG (z, P)/RG (z, P)	Weighted	...	...	>1.9	...
GPSRG (z, P)/RG (z, P)	Median	...	<0.8	<0.9	<1.7
GPSQSR (z)/QSR (z, P)	Straight	...	0.31 ± 0.21	0.75 ± 0.21	0.21 ± 0.16
GPSQSR (z)/QSR (z, P)	Weighted	<0.2	0.24 ± 0.09	0.63 ± 0.16	>0.5
GPSQSR (z)/QSR (z, P)	Median	<0.3	0.44 ± 0.41	0.32 ± 0.17	0.34 ± 0.29
BLGR (z, P)/NLRG (z)	Straight	5.50 ± 2.24	4.12 ± 1.05	1.22 ± 0.20	0.67 ± 0.32
BLRG (z, P)/NLRG (z)	Weighted	4.49 ± 1.62	3.56 ± 0.76	1.02 ± 0.16	0.53 ± 0.16
BLRG (z, P)/NLRG (z)	Median	3.74 ± 1.51	4.16 ± 1.38	2.07 ± 0.56	1.28 ± 0.54
FRII (z, P)/FRI (z, P)	Straight	<1.3	>2.9	5.12 ± 1.23	2.82 ± 0.62
FRII (z, P)/FRI (z, P)	Weighted	<1.5	1.76 ± 0.26	5.00 ± 0.89	1.52 ± 0.19
FRII (z, P)/FRI (z, P)	Median	1.32 ± 0.42	>1.5	4.85 ± 1.18	>3.9
HCP low-z QSR/RG	Straight	...	>2.8	3.95 ± 1.57	6.03 ± 2.81
HCP low-z QSR/RG	Weighted	...	>4.3	3.89 ± 1.05	3.70 ± 1.72
HCP low-z QSR/RG	Median	...	2.59 ± 1.22	2.51 ± 0.90	1.88 ± 0.96
HCP total QSR/RG	Straight	>1.2	2.65 ± 1.16	3.16 ± 1.04	2.81 ± 1.69
HCP total QSR/RG	Weighted	>2.5	4.65 ± 1.81	3.41 ± 0.78	3.16 ± 1.28
HCP total QSR/RG	Median	>1.6	1.83 ± 0.69	1.51 ± 0.48	1.25 ± 0.43

NOTES.—Col. (1): sample. The letter in parentheses designates the criteria for matching the sample, e.g., (z) means the sample was matched on redshift. Col. (2): type of mean used. Cols. (3)–(6): ratio of MFIR flux density normalized by the mean radio flux density of the samples.

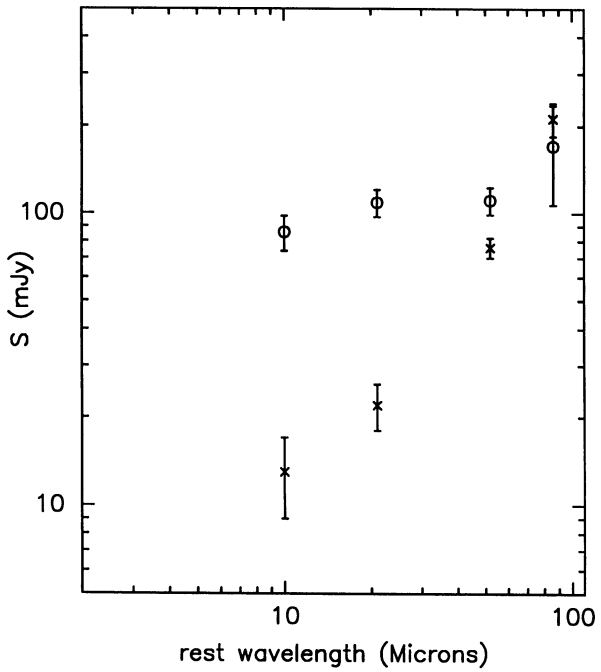

FIG. 1*a*

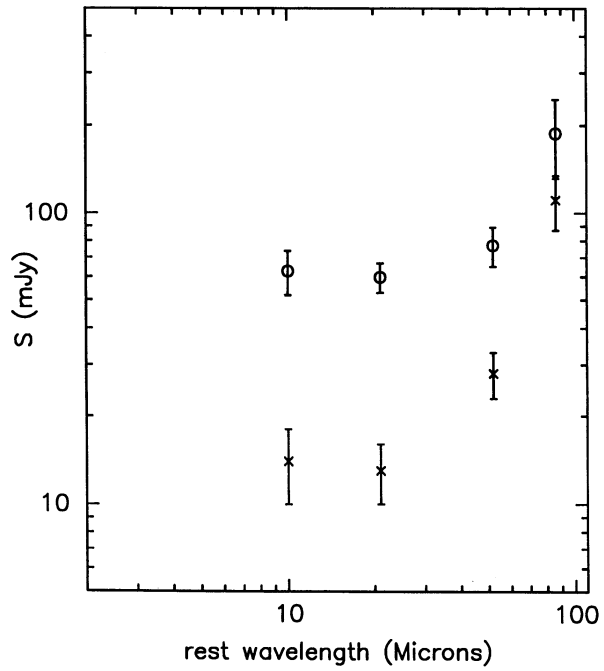

FIG. 1*b*

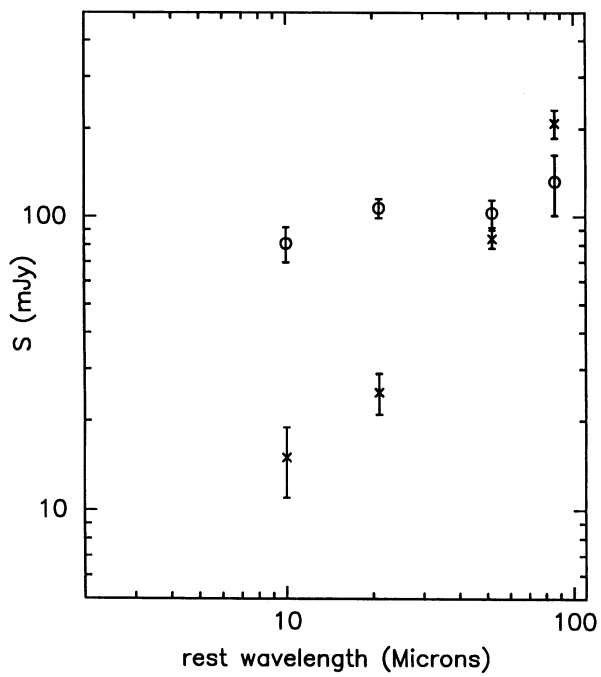

FIG. 1*c*

FIG. 1.—The measured flux densities for the NLRG (*crosses*) and BLRG (*circles*) samples plotted vs. the mean wavelength in the rest frame of the galaxies (see Tables 2 and 4 for details). (*a*) The straight mean fluxes. (*b*) The median fluxes. (*c*) The weighted mean fluxes. Note the greater strength of the BLRGs in the mid-IR and the near-equality of the two classes in the far-IR.

using the mean fluxes and the mean sample redshifts (see Table 6). Similar calculations of the radio and optical luminosities have also been made using the radio fluxes in Table 1 and the optical magnitudes (converted to fluxes following Allen 1985) as given in Spinrad et al. (1985) and private communication. In all cases we have defined the "luminosity" to be νP_ν, where P_ν is the monochromatic power per unit frequency. Note that the "total" radio luminosity integrated between 10 MHz and 100 GHz is about an order of magnitude larger than νP_ν. All calculations assume $H_0 = 75$ km s^{-1} Mpc^{-1} and $q_0 = 0$. It is clear from Table 6 that the MFIR spectral region is energetically dominant over the radio emission and is of comparable importance to the optical region. It is important to emphasize here

TABLE 6

CHARACTERISTIC LUMINOSITIES

Sample (1)	50μ (ergs s^{-1}) (2)	5 GHz (ergs s^{-1}) (3)	Optical (ergs s^{-1}) (4)
GPSRG (z, P)	3.3×10^{45}	1.1×10^{44}	2.4×10^{44}
RG (z, P)	2.3×10^{45}	9.2×10^{43}	3.3×10^{44}
GPSQSR (z)	1.0×10^{46}	4.0×10^{44}	1.6×10^{46}
QSR (z, P)	2.1×10^{46}	1.9×10^{44}	8.7×10^{45}
BLRG (z, P)	3.2×10^{44}	5.5×10^{42}	4.9×10^{44}
NLRG (z)	2.2×10^{44}	4.4×10^{42}	2.6×10^{44}
FRII (z, P)	6.3×10^{43}	4.5×10^{41}	2.5×10^{44}
FRI (z, P)	2.7×10^{43}	7.0×10^{41}	3.5×10^{44}
HCP low-z QSR	6.4×10^{45}	5.1×10^{43}	3.0×10^{45}
HCP low-z RG	1.2×10^{45}	4.4×10^{43}	2.4×10^{44}
HCP high-z QSR	1.6×10^{46}	4.3×10^{44}	1.1×10^{46}
HCP high-z RG	5.2×10^{45}	3.3×10^{44}	2.9×10^{44}
HCP total QSR	2.1×10^{46}	2.2×10^{44}	9.7×10^{45}
HCP total RG	5.3×10^{45}	1.3×10^{44}	5.1×10^{44}

NOTES.—Col. (1): sample. The letter in parentheses designates the criteria for matching the sample e.g., (z) means the sample was matched on redshift. Col. (2): characteristic observed luminosity at a rest wavelength of $\simeq 50\mu$. $L = 4\pi\langle r_{\rm lum}\rangle^2\langle \nu F_\nu\rangle$ where the averages pertain to the sample, ν is the observed frequency corresponding to a rest frequency of 6×10^{12} Hz and F_ν is the observed flux density. We adopt $H_0 = 75$ km s^{-1} Mpc^{-1} and $q_0 = 0.0$. Col. (3): characteristic observed luminosity at 5 GHz. The 178 MHz flux densities from HCP have been scaled to 5 GHz using a spectral index of -0.85. Col. (4): characteristic optical luminosity defined using the apparent optical magnitude to estimate νF_ν. See text for details.

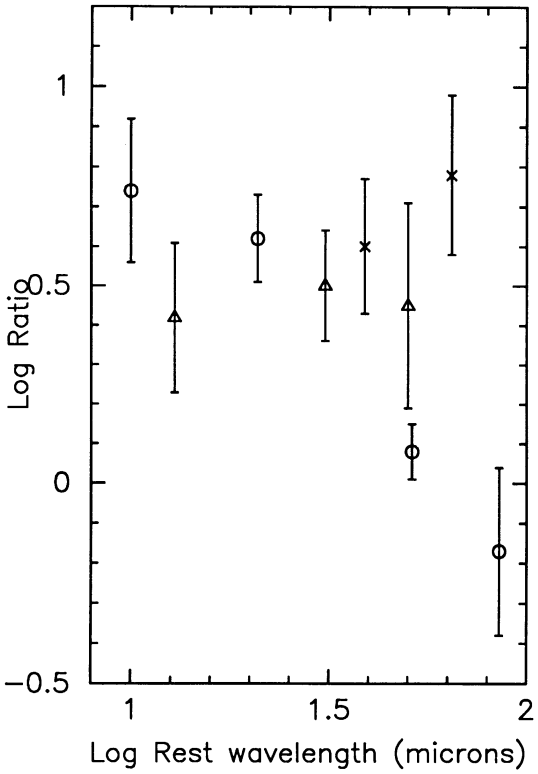

FIG. 2a

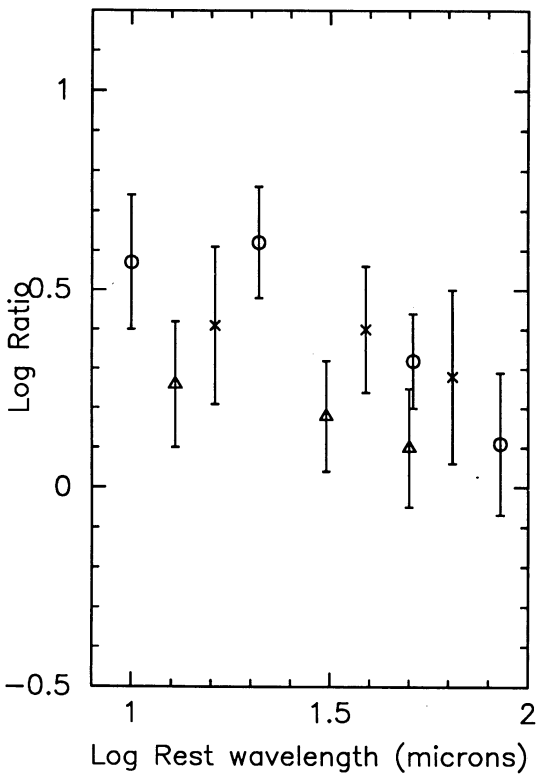

FIG. 2b

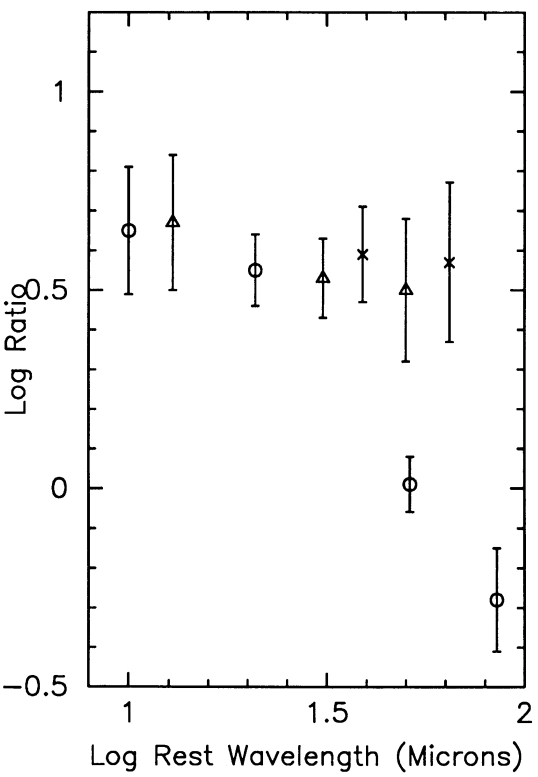

FIG. 2c

FIG. 2.—(*a*) The logarithm of the ratio of the straight mean, (*b*) median, and (*c*) weighted mean flux densities determined in three comparisons of the infrared properties of broad- and narrow-line radio-loud AGNs: BLRG/NLRG (present study, *circles*), the "low-redshift" radio-loud quasars/NLRGs (HCP, *crosses*), and "high-redshift" radio-loud quasars/NLRGs (HCP, *triangles*). In all cases the ratio is plotted vs. the mean wavelength in the rest frame of the appropriate sample. See Table 5 for details. It is not clear whether the ratio is an inverse function of rest wavelength for all samples or whether instead the HCP and present samples are intrinsically different in behavior.

that the optical emission from the NLRGs is primarily host-galaxy starlight, while both starlight and AGN light make significant contributions to the optical emission from the BLRGs (see Smith & Heckman 1989). Both the 3CR NLRGs and BLRGs are very powerful MFIR emitters (characteristic luminosities of order $10^{11}\ L_{\odot}$) compared to ordinary elliptical galaxies (e.g., Knapp et al. 1989). All these results are similar to the conclusions drawn by HCP for the high-z samples, and are also consistent with the *IRAS* surveys of GMN, Knapp et al. (1990), and Impey & Gregorini (1993).

The MFIR spectral energy distributions are characterized in Table 7 by the best fitting power-law indices α (for $P_{\nu} \propto \nu^{-\alpha}$). Using the weighted mean fluxes, the NLRGs can be adequately fitted by a power law with $\langle\alpha\rangle = 1.25 \pm 0.15$ over the rest wavelength range 10 to 86 μm (consistent with results of HCP for the $z > 0.3$ 3CR radio galaxy sample of $\langle\alpha\rangle = 1.15 \pm 0.06$ between rest wavelengths of 6 and 52 μm). The MFIR power-law index for the BLRGs is much smaller: $\langle\alpha\rangle = 0.19 \pm 0.07$ between 10 and 86 μm. This can be compared to the mean spectral index of $\langle\alpha\rangle = 0.47$ between rest wavelengths 10 and 86 μm for the radio-loud quasars in Sanders et al. (1989) and $\langle\alpha\rangle = 0.91 \pm 0.05$ in the rest wavelength range 6 to 52 μm for the $z > 0.3$ 3CR quasars in HCP.

To conclude, we find that the BLRGs have substantially larger ratios of mid-IR to radio emission than the NLRGs, that the ratio of far-IR to radio emission is similar in the two classes, that the MFIR spectral energy distribution is much flatter in the BLRGs than the NLRGs, and that the behavior of the MFIR in these low-redshift AGNs may differ from that of the more powerful high-z objects studied by HCP.

4.2. *Fanaroff-Riley Classes*

The outcome of our SUPERSCANPI analysis of the FRI and FRII samples is given in Tables 4 and 5 and plotted in Figure 3. The primary result is that the FRII sample has been convincingly detected (better than 5 σ) at 25, 60, and 100 μm.

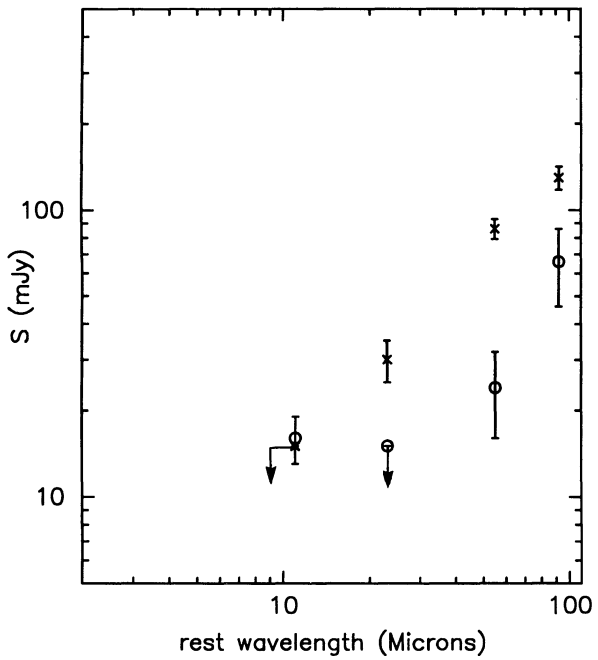

FIG. 3a

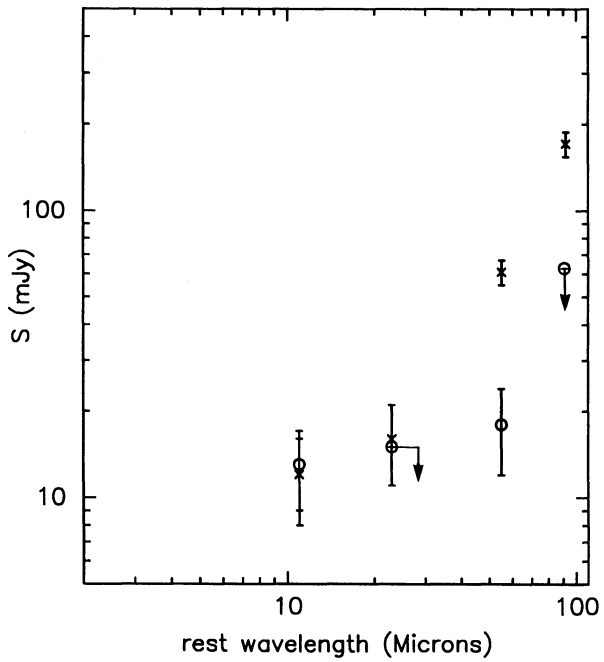

FIG. 3b

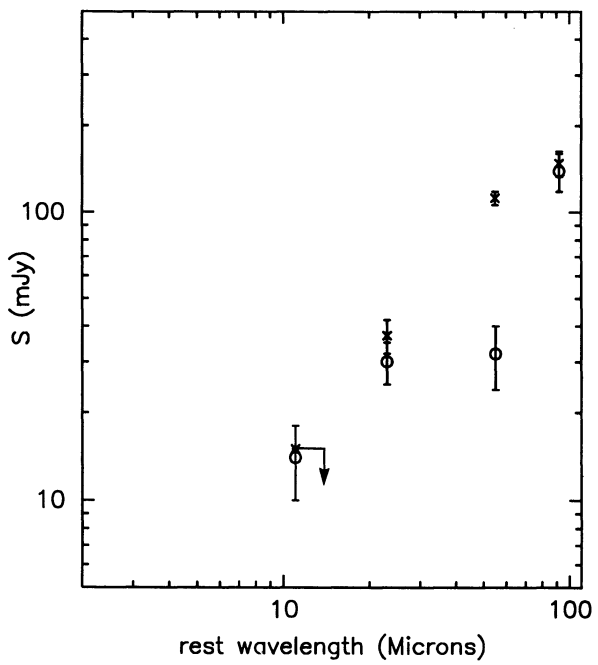

FIG. 3c

FIG. 3.—The measured flux densities for the FRII (*crosses*) and FRI (*circles*) samples plotted vs. the mean wavelength in the rest frame of the galaxies (see Tables 2 and 4 for details). (*a*) The straight mean fluxes. (*b*) The median fluxes. (*c*) The weighted mean fluxes. Note the generally stronger MFIR emission from the FRII's.

In contrast, the FRI sample is only marginally detected at 12, 60, and 100 μm. Using the detections at 60 and 100 μm, we conclude that the average FRII is brighter than the average FRI by a factor of 2.7 ± 0.6. Since the mean radio flux was a factor 1.4 times larger for the FRI sample, the mean MFIR-to-radio flux ratio is 3.8 ± 0.8 times higher for the FRII's.

The characteristic luminosities in the MFIR, radio, and optical for the FRI and FRII samples are given in Table 6. The MFIR luminosity substantially exceeds that in the radio (especially for the FRII sample) but is a bit less than the optical luminosity of the host galaxy (especially for the FRI sample). The MFIR characteristic luminosities of the FRIs ($\approx 7 \times 10^9$

TABLE 7

MFIR SPECTRAL INDICES

Sample (1)	Mean Type (2)	α (3)	$\Delta\lambda$ (rest) (4)
GPSQSR (z)	Median	1.03 ± 0.26	13–51μ
GPSQSR (z)	Straight	0.92 ± 0.40	13–51μ
GPSQSR (z)	Weighted	0.98 ± 0.30	13–51μ
QSR (z, P)	Median	0.88 ± 0.20	6–51μ
QSR (z, P)	Straight	1.06 ± 0.45	13–51μ
QSR (z, P)	Weighted	0.78 ± 0.33	6–31μ
BLRG (z, P)	Median	0.46 ± 0.23	10–86μ
BLRG (z, P)	Straight	0.27 ± 0.09	10–86μ
BLRG (z, P)	Weighted	0.19 ± 0.07	10–86μ
NLRG (z)	Median	0.93 ± 0.36	10–86μ
NLRG (z)	Straight	1.31 ± 0.17	10–86μ
NLRG (z)	Weighted	1.25 ± 0.15	10–86μ
FRII (z, P)	Median	1.27 ± 0.23	11–92μ
FRII (z, P)	Straight	1.07 ± 0.10	23–92μ
FRII (z, P)	Weighted	1.03 ± 0.19	23–92μ
FRI (z, P)	Straight	2.0 ± 0.9	55–92μ
HCP QSR (z, P)	Median	0.71 ± 0.16	6–52μ
HCP QSR (z, P)	Straight	1.12 ± 0.10	6–52μ
HCP QSR (z, P)	Weighted	0.91 ± 0.05	6–52μ
HCP RG (z, P)	Median	1.10 ± 0.37	13–52μ
HCP RG (z, P)	Straight	1.05 ± 0.35	13–52μ
HCP RG (z, P)	Weighted	1.15 ± 0.06	13–52μ

NOTES.—Col. (1): sample. The letter in parentheses designates the criteria for matching the sample, e.g., (z) means the sample was matched on redshift. Col. (2): type of mean used. Col. (3): spectral index and 1 σ error calculated using a least-squares linear fit to log flux density vs. log frequency. Col. (4): range of wavelength in rest frame of sample over which the spectral index is calculated.

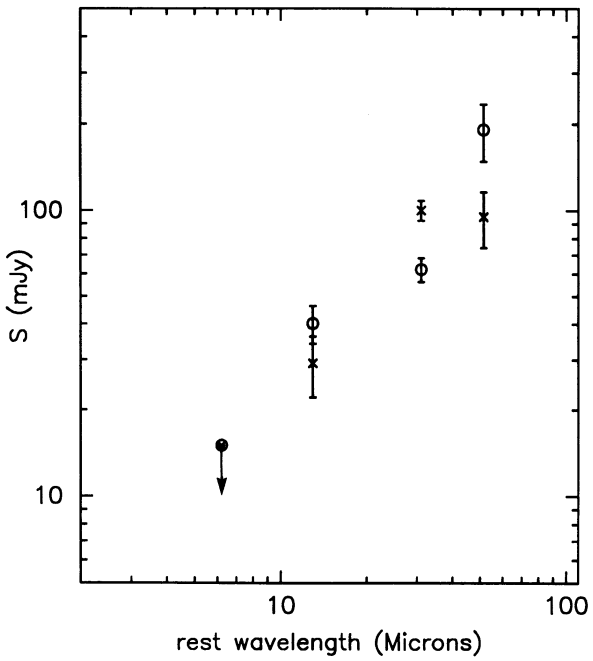

FIG. 4*a*

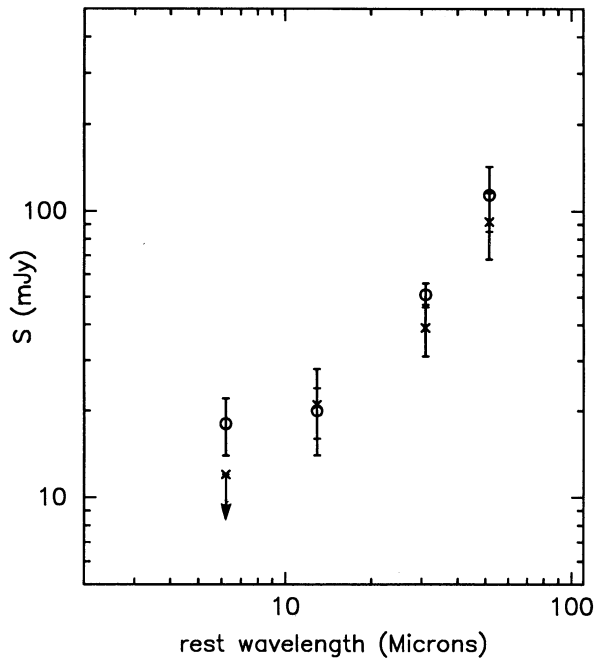

FIG. 4*b*

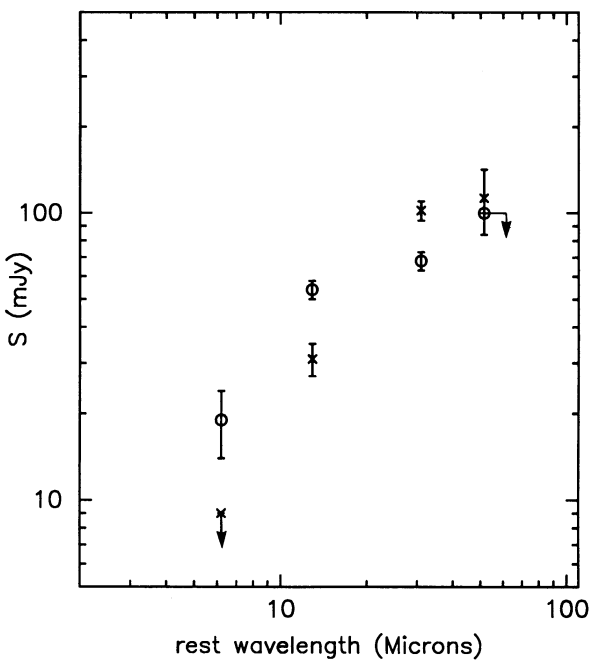

FIG. 4*c*

FIG. 4.—The measured flux densities for the *z*-matched GPS-CSS quasar (*crosses*) and non–GPS-CSS quasar (*circles*) samples plotted vs. the mean wavelength in the rest frame of the quasars (see Tables 2 and 4 for details). (*a*) The straight mean fluxes. (*b*) The median fluxes. (*c*) The weighted mean fluxes. The two samples have similar MFIR fluxes to within a factor of ≈ 2.

$L_\odot$) and FRIIs ($\approx 1.7 \times 10^{10}\ L_\odot$) are both large compared to the typical MFIR luminosity of normal giant elliptical galaxies.

The MFIR spectral energy distribution for the FRII's can be represented by a power-law index $\alpha = 1.03 \pm 0.19$ between rest wavelengths of 23 and 92 μm. This slope is consistent with both the result in § 4.1 for the 3CR NLRG sample and with the results reported in HCP for the $z > 0.3$ 3CR radio galaxy sample. We have only minimal constraints on the MFIR spectral energy distribution for the FRI's (e.g., $\alpha = 2.0 \pm 0.9$ between 54 and 92 μm). See Table 7 for details.

Note that while good optical spectra are not uniformly available for our sample of FRII's, none of them are known to us to be BLRGs. Given the small fraction of BLRGs in the 3CR catalog in this range of radio power (see above and Lawrence 1991), we expect that the MFIR properties of the FRII sample are representative of the NLRG rather than BLRG population. This is consistent with the overall similarity in the MFIR spectral energy distributions between our NLRG and FRII samples (see above).

4.3. *Gigahertz-peaked Spectrum & Compact Steep Spectrum Sources*

The outcome of our SUPERSCANPI analysis of the GPS-CSS and comparison samples is given in Tables 4 and 5 and displayed (quasars only) in Figure 4. For the quasars, both the GPS-CSS and comparison samples are detected at 25, 60, and 100 μm. Within the uncertainties, we can conclude that the GPS-CSS quasars and non–GPS-CSS quasars have mean and median MFIR fluxes that are similar to within a factor of about 2 (Tables 4 and 5). Since the GPS-CSS sample had a mean 5 GHz flux about a factor of 2 higher than that of the comparison sample, the mean MFIR-to-radio flux ratio is about a factor of 2 lower for the GPS-CSS quasars than for the comparison sample. In the case of the galaxies, there are only marginal detections of the GPS-CSS sample at 60 μm and of the comparison sample at 60 and 100 μm. We can only say that the mean fluxes at 60 μm for the GPS-CSS and comparison galaxies are similar to within a factor of about 2 or 3 (which is also consistent with the results at 100 μm).

The characteristic MFIR luminosities for the GPS-CSS and non–GPS-CSS quasar samples are several $\times 10^{12}\ L_\odot$, comparable to the optical luminosities but exceeding the character-

istic radio luminosities by one and one-half to two orders of magnitude (see Table 6). The characteristic MFIR luminosities of the GPS-CSS and non–GPS-CSS radio galaxies are nearly as large (almost 10^{12} $L_{\odot}$), much larger than either the characteristic optical or radio luminosities (Table 6). We have only weak constraints on the MFIR spectral energy distributions for the GPS-CSS quasars, which appear to be similar to those of the other classes of radio-loud AGNs investigated here (see Table 7).

5. DISCUSSION

5.1. *The Origin of the MFIR: General Considerations*

Viable models for the MFIR radiation from radio-loud AGNs include thermal emission from dust heated by the AGN (e.g., PK92, PK93; Sanders et al. 1989; Rowan-Robinson & Crawford 1989; Kraemer & Harrington 1986; Netzer & Laor 1993), thermal emission from dust heated by a starburst (e.g. GMN; Mirabel, Sanders, & Kazes 1989; Mazzarella et al. 1993; Impey & Gregorini 1993), and nonthermal emission (e.g., Zdziarski 1986; Band & Malkan 1989). The last model is clearly relevant to the radio core–dominated and blazar class of radio-loud AGN in which it is believed that Doppler-boosted emission from a relativistic jet viewed nearly end-on dominates the overall spectrum (see Antonucci 1993 and references therein). While we have excluded objects in which the integrated radio continuum properties are dominated by a blazar/core component from the samples we have considered, such a component may make a detectable contribution to the MFIR emission of the BLRGs and lobe-dominated radio-loud quasars (since these objects still have relatively strong radio cores).

In contrast, there is now rather convincing evidence that the MFIR continuum in typical radio-quiet AGNs is thermal in nature. As recently reviewed in detail by Barvainis (1990), this evidence includes the relatively large sizes of the MFIR sources in nearby Seyferts, the lack of MFIR variability, the low or vanishingly small polarization in the MFIR, the steep spectral cutoff in the sub-millimeter spectral region, the "universal" minimum in the quasar spectral energy distribution near a rest wavelength of about 1 μm, the behavior of the 10 μm silicate absorption feature, and the association between far-IR emission and the presence of molecular gas.

The situation for the class of "lobe-dominated" radio-loud AGNs considered in this paper is less clear. Since the UV through far-IR spectral energy distribution for radio-loud quasars (excluding blazars) is essentially identical to that in radio-quiet quasars (Sanders et al. 1989), it seems most likely that the MFIR has the same origin as in the radio-quiet quasars and so is predominantly thermal. On the other hand, radio-loud quasars (even the radio lobe–dominated ones considered in the present paper) have strong compact radio cores, and it is possible that these are just the self-absorbed low-frequency tails of a nonthermal nuclear MFIR source. Antonucci, Barvainis, & Alloin (1990) and Knapp & Patten (1991) have argued otherwise for at least some objects (but see the discussion in § 5.2 below).

5.2. *Broad-Line versus Narrow-Line Objects*

The results presented in § 4.1 above and in HCP can be summarized as follows (see Table 5 and Figs. 1 and 2).

1. In the mid-IR (that is, below a rest wavelength of $\approx$40 μm), all the samples of broad-line objects in the 3CR sample are significantly stronger emitters than are the narrow-line objects (by a factor of about 3 to 5).

2. In the far-IR (that is, above a rest wavelength of about 50 μm) the situation appears more complex. The 3CR low-luminosity ($z < 0.3$) broad- and narrow-line objects have fluxes that agree to within a factor of 2, while the more luminous ($z > 0.3$) 3CR broad-line objects remain significantly stronger (factor of 2 to 5) emitters than their $z > 0.3$ narrow-line counterparts.

The stronger mid-IR emission in the broad-line objects is at least qualitatively consistent with models for optically thick thermal emission from a circumnuclear torus or warped disk that is primarily heated by the optical and UV radiation of the central source. The most detailed such published models are those of PK92, who have used a two-dimensional radiative transfer calculation to predict the thermally reradiated IR spectra of dusty tori as a function of viewing angle and torus geometry. The torus is optically thick in the mid-IR and (since it is highly nonspherical) radiates anisotropically. PK93 found that typical observed AGN continua at wavelengths greater than about 25 μm are significantly brighter than the simple torus models predict and therefore conclude that this far-IR emission must then come primarily from optically thin regions exterior to the torus itself.

The model adopted by PK93 as best able to reproduce the mid-IR spectra of typical low-redshift AGNs implies a ratio in the intensity of radiation from a face-on torus versus an edge-on torus of about 20:1 in the 10–20 μm range. The expected values of the mean flux ratios for real samples of broad-line versus narrow-line objects will be considerably smaller than the above extreme value, since the tori will be viewed over the full range of appropriate inclinations. In the context of the standard unification model, the relative numbers of NLRGs and BLRGs in the 3CR sample ($\approx$5:1) implies that the BLRGs are those objects in which the line of sight lies within about 34° of the polar axis of the torus. Such a geometry is almost exactly equivalent to the standard torus model in PK93 in which the broad-line AGNs are those viewed from within 31° of the torus polar axis. Averaging the predicted MFIR anisotropy factor over the expected range of viewing angles ($\cos i = 0$ to 0.83 for the NLRGs and $\cos i = 0.83$ to 1.0 for the BLRGs) then implies that the ratio of the mean BLRG/NLRG MFIR fluxes will vary from about 2.2 at 10–20 μm to about 1.2 at 100 μm for their standard torus model. Note that the expected mean flux ratios at wavelengths >25 μm will actually be even closer to unity when the optically thin emission far-IR from the region exterior to the torus in included (see above).

At the higher MFIR luminosities probed by the samples studied by HCP, the situation changes. Here the ratio of the number of narrow-line to broad-line objects in the 3CR is significantly smaller (it is 2.4:1 for the $z = 0.3$ to 0.85 HCP sample and 1.4:1 for $z > 0.85$ HCP sample). This trend of declining fraction of narrow-line objects with increasing luminosity in the 3CR sample has been previously discussed by Lawrence (1991). The standard unification model then demands that the opening (half-) angle of the obscuring torus must increase from about 30° for the lowest luminosity objects to about 60° for the highest luminosity ones. Ed Pier (1993, private communication) has kindly run torus models whose geometry is appropriate for these highly-luminous objects (these have $a/h = 1$ in the PK92, PK93 notation). While the range in viewing angles appropriate for the broad-line objects

is now substantially larger than in the standard PK93 model, the mean anisotropy this introduces is nearly canceled out by the substantially larger solid angle over which the observed MFIR intensity is close to its "pole-on" value. Thus, the predicted ratio of the mean 10–20 μm fluxes for the quasars versus the radio galaxies remains 2.2. In fact, the predicted mean ratio remains within about 10% of this value for a large range of torus geometries (including "slender" tori in which the optical depth in the radial direction is significantly greater than in the vertical direction).

These predictions can be compared with the results shown in Table 5 and Figures 1 and 2. The actual flux ratios (both means and medians) are between 2.5:1 and 6:1 for the various samples in the rest wavelength range between 10 and 20 μm. This is about a factor of 2 larger than predicted by the PK models. Given the robustness of the model prediction (see above) it is unclear how to account for this discrepancy. The PK models also cannot account for the significantly stronger far-IR emission in the more luminous broad-line objects (3CR quasars) studied by HCP. As HCP concluded, either the 3CR quasars are intrinsically stronger far-IR emitters than the 3CR radio galaxies (in which case the simple Barthel-style unification model cannot be correct), or the far-IR emission (not just the mid-IR) must be radiated anisotropically. This may be difficult to reconcile with purely thermal models for the far-IR for these objects, because of the very large gas mass implied for an optically thick far-IR source of such enormous luminosity.

This may suggest that a beamed nonthermal (blazar) component makes a significant contribution to the MFIR in some lobe-dominated 3CR quasars. The data discussed by Antonucci et al. (1990) and Knapp & Patten (1991) imply that this cannot be the case in general. However, recent sub-millimeter observations of a subsample of the 3CR quasars in the HCP sample by Antonucci (1993, private communication) and collaborators show that some of these are strong sub-millimeter continuum sources. This suggests that there may be spectral continuity (and hence a physical connection) between the radio core and the far-IR source. Further sub-millimeter observations of BLRGs and lobe-dominated quasars are clearly important in this regard.

As noted above, the decline in the relative numbers of narrow-line objects in the 3CR with increasing luminosity can be reconciled with the standard unification scheme only if the geometry of the obscuring region also changes with luminosity. It is possible that the apparent dependence of the far-IR properties on luminosity may be related to this changing geometry. For a simple obscuring torus model, the NLRGs in the 3CR at $z < 0.3$ are viewed over a wide range in polar angles ($\approx 30°$ to 90°), while the most luminous 3CR NLRGs (e.g., at $z > 1$) must all be viewed from within about 30° of the torus equatorial plane. Perhaps the far-IR source becomes optically thick only when viewed near to its equatorial plane. This speculation clearly needs to be investigated quantitatively.

It is also possible that the far-IR emission in some 3CR quasars and radio galaxies is produced by more than one mechanism. For example, there may be both an anisotropic nonthermal source (associated with the radio jets?) and a more nearly isotropic thermal source (reradiated AGN and/or starburst light). Perhaps the former becomes increasingly important in the objects of higher radio luminosity. This would be expected if the covering factor of the thermal far-IR source declined with radio luminosity (which is in fact suggested by the declining fraction of narrow-line objects at higher luminosity), or if the thermal far-IR source were powered by a starburst rather than by the AGN. We will return to these issues in § 5.5 below.

5.3. *Fanaroff-Riley Classes*

We have shown that FRII radio galaxies have significantly higher ratios of MFIR to radio luminosities (factor ≈ 4) than FRI radio galaxies with similar radio powers and redshifts. It is, of course, possible that the MFIR emission has the same origin in the two types of radio galaxies and is simply stronger in the FRII's. However, we think it is possible that the MFIR could have a qualitatively different origin in the two classes, as we now explain.

There is now ample evidence that nearby ($z < 0.3$) FRI and FRII radio galaxies are distinct phemonena with—at best—only an indirect relationship to one another. The host galaxies of FRI's are more optically luminous (see Smith & Heckman 1989; Prestage & Peacock 1988; Owen & Laing 1989), have larger stellar velocity dispersions and rotate less rapidly (Smith et al. 1990), are redder (Smith & Heckman 1989), are less likely to be morphologically peculiar (Heckman et al. 1986; Baum & Heckman 1989; Smith & Heckman 1989), inhabit regions of higher galaxy density (Longair & Seldner 1979; Prestage & Peacock 1988), and exhibit less cosmic evolution (see Hill & Lilly 1991). The optical manifestations of the AGN are also different in the two classes of radio galaxies: while FRII's generally have strong, high-ionization (Seyfert-type) optical emission lines, the FRI's have weak, low-ionization (LINER-type) emission lines (Hine & Longair 1979; Baum et al 1992; Zirbel et al. 1994). The ionized nebulae associated with the FRII's often appear to be kinematically disturbed disklike systems with a rotation axis that roughly aligns with the radio axis (Simkin 1979; Heckman et al. 1985; Baum et al. 1992). The ionized nebulae associated with FRI's appear to be kinematically disordered with large line-of-sight velocity dispersions, but little organized large-scale shear or rotation (Baum et al. 1992), similar to the nebulae associated with cluster-dominant giant ellipticals immersed in cooling flows (see Heckman et al. 1989).

Baum, Heckman, & van Breugel (1992) suggested that all these differences could be accomodated by a picture in which: 1) the FRI's are giant ellipticals located at the centers of clusters and groups and possibly "fueled" by a cooling flow in the associated intracluster medium, and 2) the FRII's are recent or ongoing interactions or mergers of massive galaxies in which at least one of the participants is a disk galaxy.

The difference in the MFIR properties of the two classes can also be incorporated into this picture. Given the causal connection between galaxy interactions and starbursts (see Heckman 1990 and references therein) the large incidence rate of morphological peculiarities in the FRII host galaxies might then imply that much of the MFIR emission is powered by a starburst—as GMN, Mirabel et al. (1989), Mazzarella et al. (1993), and Impey & Gregorini (1993) have argued (but see § 5.5 below). By contrast, the MFIR emission of the FRI's may be associated with the intracluster medium rather than the AGN itself. A typical low-z FRI host galaxy appears to be the otherwise normal giant elliptical or cD galaxy near the center of a galaxy cluster of average Abell richness class 0 (see Hill & Lilly 1991). Wise et al. (1993) have recently shown that—independent of the presence of a radio galaxy—the cores of such clusters are detected by *IRAS* with a characteristic 60 μm luminosity of $\nu P_\nu \approx 7.5 \times 10^9\ L_\odot$ within a region whose char-

acteristic diameter is about 600 kpc. This characteristic luminosity is similar to our value for the FRI's, and a diameter of 600 kpc corresponds to about 5′ (similar to the *IRAS* beam) at the mean redshift of our FRI sample. Given the low signal-to-noise ratio in the current data, we cannot convincingly determine whether the "composite" FRI source produced by SUPERSCANPI is resolved by *IRAS* at 60 or 100 μm.

Whatever its origin, the weakness of the far-IR emission from the FRI's suggests that the ratio of AGN radiant luminosity to jet mechanical energy flux could be abnormally small in the FRI's. This is also consistent with the deficiency in optical line emission in FRI's relative to comparably radio luminous FRII's discovered by Zirbel et al. (1994). A deficiency in the production of radiant energy in the nuclei of FRI's would support the speculation that their central engine may be qualitatively different. For example, FRI's may be powered by the spin-down of a rotating supermassive black hole surrounded by an ion-supported torus (see Rees et al. 1982; Phinney 1983). Alternatively, the high ratio of radio power to far-IR continuum and optical line emission in FRI's may imply that the efficiency of the conversion of jet mechanical energy into radio emission is higher in the FRI's than in FRII's (see Zirbel et al. 1994).

5.4. *Gigahertz-peaked Spectrum and Compact Steep Spectrum Sources*

Our results imply that there are no strong differences (greater than a factor of several) between the mean MFIR fluxes of GPS and CSS radio sources on the one hand and lobe-dominated radio sources of similar radio flux and radio power on the other. At least for the quasars, this is also true for the mean optical fluxes relative to the mean MFIR and radio fluxes (the CSS-GPS quasars do not appear significantly different from the lobe-dominated radio-loud quasars). We would like to discuss two implications of these results.

First, this overall similarity in the ratio of the radio to the MFIR (or optical) power argues against a strong environmental dependence of the efficiency of the conversion of jet kinetic energy into radio emission. Such a dependence has been suggested on largely theoretical grounds by a number of different authors (see Gopal-Krishna & Wiita 1991; De Young 1993). Given a set of AGNs with the same central engine output (photon luminosity and jet kinetic energy flux), this theoretical argument would predict that the radio power would be largest for those AGNs immersed in the densest gaseous environment. Insofar as the GPS and CSS radio sources are thought to result from powerful radio jets propagating through exceptionally dense circumnuclear gas (see Fanti et al. 1990b; O'Dea et al. 1991), a GPS or CSS source of a given radio power would therefore have been predicted to be associated with an intrinsically less luminous AGN than would another equally radio-powerful non–GPS-CSS AGN. In this case, it is surprising that the GPS-CSS samples do not exhibit any significant relative deficiency in their MFIR or optical continuum emission.

Another possibility is that the exceptionally dense circumnuclear gas associated with CSS and GPS sources is dusty and will result in an abnormally large fraction of the optical ultraviolet (OUV) light from the quasar being absorbed and reradiated in the MFIR. In this case, we would expect that the GPS and CSS quasars would have unusually large MFIR/OUV flux ratios. This does not appear to be the case in our samples. In fact, the ratio of the mean MFIR/OUV fluxes is actually about 4 times lower for the GPS-CSS quasars (see Table 6), so any connection between the gas responsible for confining the GPS and CSS radio sources and dusty material ostensibly responsible for the MFIR emission is not demonstrated by our data.

Finally, one natural interpretation of our results is that the GPS-CSS sources do not in fact reside in regions of abnormally high gas density but instead owe their small sizes to their relative youth. While there are a variety of indirect arguments that favor a high-density environment (Fanti et al. 1990a), this alternative explanation cannot be excluded.

5.5. *The Power Source for the Mid- and Far-Infrared*

We show in Figure 5 that the characteristic MFIR and radio luminosities of the various radio-loud AGN samples studied here and in HCP correlate well with one another over a range of about three orders of magnitude in luminosity. For the objects where the bulk of the optical continuum is produced by the AGN (the quasars and BLRGs) rather than by the host galaxy (all the other radio galaxies), there is also a good correlation between the MFIR and optical luminosity (Figure 6). These results are consistent with those of many previous investigations of radio-loud nonblazar AGNs (e.g., Neugebauer et al. 1986; GMN; Sanders et al. 1989; Knapp et al. 1990; Impey et al. 1990; HCP; Impey & Gregorini 1993).

The simplest interpretation of this result is that the bulk of the MFIR emission in radio galaxies and radio-loud quasars is powered directly by the AGN. GMN, Mirabel, Sanders, & Kazes (1989), Impey & Gregorini (1993), and Mazzarella et al. (1993) have suggested that the MFIR in radio-loud AGNs may be powered by a circumnuclear starburst that is only indirectly related to the AGN. In this case, the correlations seen in Figures 5 and 6 are somewhat surprising, since they would demand that not only does the starburst luminosity scale with the power of the AGN, but (at least in the case of the quasars and BLRGs) the starburst MFIR luminosity must be fortuitously nearly equal to the optical-UV luminosity of the AGN. This seems unlikely to us.

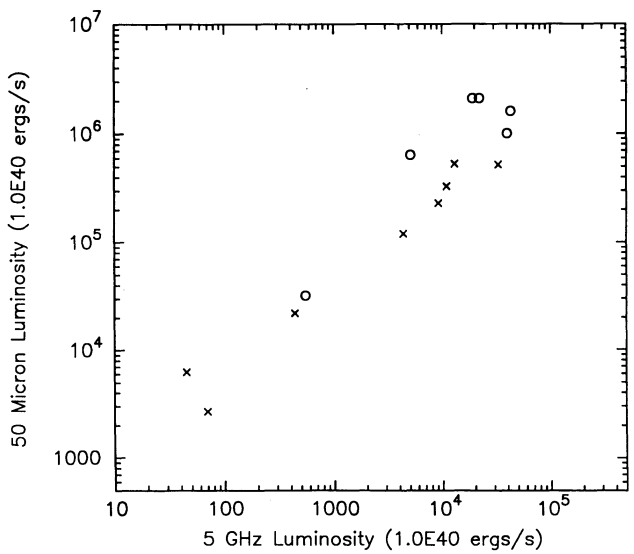

FIG. 5.—The far-IR characteristic luminosity at a rest wavelength of ≈ 50 μm plotted vs. the radio characteristic luminosity at 5 GHz for all the samples of radio-loud quasars (*circles*) and radio galaxies (*crosses*) in the present paper and in HCP. See Table 6 and HCP for details. Note the strong correlation.

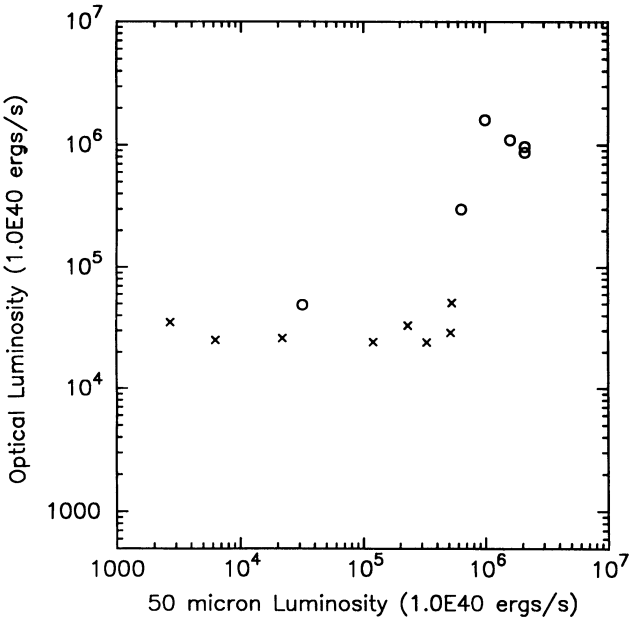

FIG. 6.—The optical characteristic luminosity plotted vs. the radio characteristic luminosity at 5 GHz for all the samples of radio-loud quasars (*circles*) and radio galaxies (*crosses*) in the present paper and in HCP. See Table 6 and HCP for details. Note the good correlation for the quasars and the roughly constant optical (host galaxy) luminosity for the radio galaxies.

That said, it may still be the case that starbursts power a significant fraction of the MFIR emission of particular radio-loud AGNs—e.g., those radio galaxies or radio-loud quasars with very strong millimeter-wave CO emission like those studied by Mirabel et al. (1989), Mazzarella et al. (1993), and Scoville et al. (1993). Note that Alloin et al. (1992) have found that some radio-quiet quasars can also have strong CO emission. Moreover, it seems clear that the less powerful the AGN, the more likely that sources other than the AGN will make detectable contributions to the integrated MFIR emission. For example, we cannot exclude the possibility that starbursts make important contributions to the MFIR emission from typical low-redshift FRII radio galaxies. This would be consistent with the clear systematic increase in the ratio of far-IR/radio power as the radio power decreases for the radio galaxy samples ($L_{\rm FIR} \propto L_{\rm Rad}^{0.7}$—see Fig. 7). There is no such clear trend for the quasar samples, however. It may also be the case that the very weak MFIR emission from FRI galaxies is not powered by the AGN at all but is instead related to their status as galaxies located near the centers of galaxy clusters (see § 4.2).

6. SUMMARY

We have used the *IRAS* database and the SUPERSCANPI algorithm to compare the class-average MFIR properties of several of the principal types of radio-loud active galaxies (excluding the "core-dominated" flat–radio spectrum blazar sources).

First, we have compared a sample of low-redshift ($0.05 < z < 0.3$) BLRGs from the 3CR to a sample of 3CR NLRGs which have been approximately matched in redshift and low-frequency radio flux. We find that the ratio (BLRG/NLRG) of the mean MFIR flux for our samples is a strong function of wavelength, ranging from about 5:1 at a rest wavelength of 10 μm to essentially unity at 90 μm. This result is compared to the predictions of the standard "unified" model in which NLRGs and BLRGs are drawn from the same parent population but are viewed more nearly perpendicular or parallel to the radio axis, respectively. Consistency with this model demands that the infrared emission is radiated anisotropically in the mid-infrared but isotropically in the far-infrared. This is at least qualitatively compatible with recent models by PK92 and PK93 for the mid-infrared emission from a central "obscuring torus." Comparison of these results with the similar study of 3CR radio galaxies and quasars at $z > 0.3$ by HCP suggests that the MFIR properties of radio-loud AGNs may depend on luminosity: at the higher levels of radio power studied by HCP, the quasars remained stronger emitters than the radio galaxies even in the far-IR. As discussed by HCP, this result may be difficult to reconcile simultaneously with a thermal origin for the far-IR and the popular quasar/radio galaxy unification picture proposed by Barthel (1989).

Second, we have compared the MFIR emission between samples of FRI and FRII galaxies with matched redshifts and radio fluxes. The FRII's are convincingly detected ($> 5\,\sigma$) at 25, 60, and 100 μm, while the FRI's are only marginally detected. The FRII's are about four times stronger MFIR emitters than FRI's with the same radio flux and luminosity. Since typical FRI's are giant ellipticals in the central regions of moderately rich clusters of galaxies, and since the typical far-IR luminosity of an FRI galaxy is similar to that of the core of a galaxy cluster, it is possible that much of the far-IR emission in the FRI sample may not be powered by the AGN at all. This is consistent with the speculation that FRI's may have central engines with abnormally small ratios of radiant luminosity to jet kinetic energy flux. Alternatively, it might imply that FRI radio sources have an unusually high efficiency for converting jet kinetic energy into radio synchrotron emission.

Third, we have compared samples of GPS sources and CSS sources to samples of normal steep–radio spectrum radio galaxies and quasars with matched radio powers and redshifts. In this case, we have matched the radio powers at 5 GHz, where the radio emission is optically thin in the GPS and CSS sources. The GPS-CSS and comparison samples have mean MFIR fluxes that agree to within a factor of about 2. Moreover, the mean optical fluxes of the GPS-CSS quasars and the

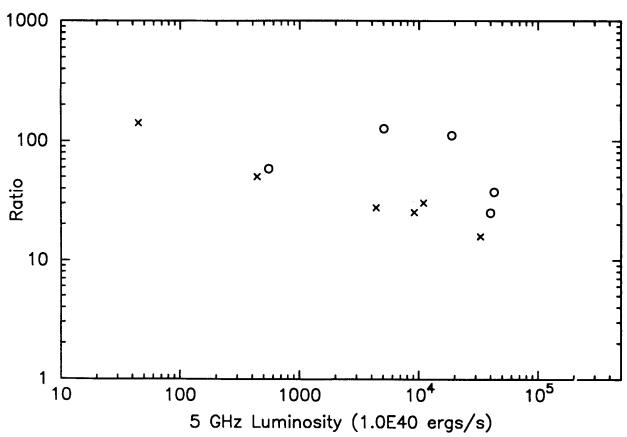

FIG. 7.—The ratio of the far-IR and radio characteristic luminosities plotted vs. the characteristic radio luminosity for the samples of radio-loud quasars (*circles*) and radio galaxies (*crosses*) studied in the present paper and in HCP (see Table 6 for details). The ratio declines systematically with radio power for the radio galaxies but not for the quasars. We have excluded the FRI radio galaxy sample from this figure, since it seems likely that the far-IR in these galaxies is not powered by the AGN (see text).

comparison sample of quasars also agree to within a factor of 2. These results suggest that the efficiency with which jet kinetic energy is converted into synchrotron radiation may not be a strong function of the density of the gas through which the jet propagates (contrary to some theoretical suggestions). There is also no evidence that the dense gas that apparently confines the GPS-CSS sources is related to the material giving rise to the MFIR continuum.

Finally, we find that the mean far-IR luminosities are well correlated with the mean radio luminosities for all the samples of radio galaxies and radio-loud quasars we have investigated, which together span a range of about three orders of magnitude in radio and far-IR luminosity. For the BLRGs and quasars, the mean far-IR luminosity also correlates well with the mean UV-optical luminosity. The monochromatic power (νP_ν) at a rest wavelength of 50 μm is typically about one and one-half to two orders of magnitude greater than the monochromatic power in the optically thin part of the radio spectrum and (in the BLRGs and quasars) is similar to the UV-optical monochromatic power. These results are most naturally understood if the MFIR is primarily powered by the same "central engine" as the radio source. However, other energy sources for the MFIR (e.g., starbursts, the intracluster medium, etc.) may be significant in at least some radio galaxies of modest radio power. This is suggested by a systematic increase in the ratio of far-IR to radio power with decreasing radio power for the radio galaxies.

We would like to thank Ski Antonucci, Julian Krolik, and Ed Pier for useful discussions of many of the issues and ideas presented in this paper. We especially thank Ed Pier for some specific calculations of the aspect angle–dependence of the infrared spectral energy distribution expected for dusty tori in his models with Krolik. This research was supported in part by a NASA ADP grant to T. M. H. (NAG 5-1368) and by funds provided by the STScI Visitor Program to C. P. O. and S. A. B. in support of E. L. IPAC is funded by NASA as part of the *IRAS* extended mission under contract to JPL.

REFERENCES

Allen, C. W. 1985, Astrophysical Quantities (London: Anthlone)
Alloin, D., Barvainis, R., Gordon, M., & Antonucci, R. 1992, A&A, 265, 429
Antonucci, R., 1993, ARA&A, 31, 473
Antonucci, R., & Barvainis, R. 1990, ApJ, 363, L17
Antonucci, R., Barvainis, R., & Alloin, D. 1990, ApJ, 353, 416
Band, D., & Malkan, M. 1989, ApJ, 345, 122
Barthel, P. 1989, ApJ, 336, 606
Barvainis, R. 1992, in Testing the AGN Paradigm, ed. S. Holt, S. Neff, & C. M. Urry (New York: AIP), 129
Baum, S., & Heckman, T. 1989, ApJ, 336, 702
Baum, S., Heckman, T., & van Breugel, W. 1992, ApJ, 389, 208
Beichman, C., Neugebauer, G., Habing, H., Clegg, P., & Chester, T. 1984, *IRAS* Catalogs and Atlases: Explanatory Supplement (Pasadena: JPL)
Bennett, A. 1962, MmRAS, 68, 163
Blandford, R. 1991, in Active Galactic Nuclei (1990 Saas-Fee Lectures), ed. R. Blandford, H. Netzer, & L. Woltjer (Dordrecht: Kluwer)
Bridle, A., & Perley, R. 1984, ARA&A, 22, 319
Caganoff, S. 1989, Ph.D. thesis, Australian National Univ.
Dahari, O., & DeRobertis, M. 1988, ApJS, 67, 249
De Young, D. 1993, ApJ, 402, 95
Fanaroff, B., & Riley, J. 1974, MNRAS, 167, 31P
Fanti, C., Fanti, R., de Ruiter, H., & Parma, P. 1987, A&AS, 69, 57
Fanti, C., Fanti, R., O'Dea, C., & Schilizzi, R. 1990a, ed. Compact Steep-Spectrum and GHz-Peaked Spectrum Radio Sources (Bologna: Istituto di Radioastronomia)
Fanti, R., Fanti, C., Schilizzi, R., Spencer, R., Rendong, N., Parma, P., van Breugel, W., & Venturi, T. 1990b, A&A, 231, 333
Golombek, D., Miley, G., & Neugebauer, G. 1988, AJ, 95, 26 (GMN)
Gopal-Krishna, & Wiita, P. 1991, ApJ, 373, 325
Grandi, S., & Osterbrock, D. 1978, ApJ, 220, 783
Heckman, T. 1990, in Paired and Interacting Galaxies, ed. J. Sulentic, W. Keel, & C. Telesco (NASA CP 3098), 359
Heckman, T., Baum, S., McCarthy, P., & van Breugel, W. 1989, ApJ, 338, 48
Heckman, T., Chambers, K., & Postman, M. 1992, ApJ, 391, 39 (HCP)
Heckman, T., Illingworth, G., Miley, G., & van Breugel, W. 1985, ApJ, 293, 83
Heckman, T., van Breugel, W., Balick, B., Miley, G., Bothun, G., Illingworth, G., Baum, S., & Smith, E. 1986, ApJ, 311, 526
Hill, G., & Lilly, S. 1991, ApJ, 367, 1
Hine, R., & Longair, M. 1979, MNRAS, 188, 111
Impey, C., & Gregorini, L. 1993, AJ, 105, 853
Impey, C., Wynn-Williams, G., & Becklin, E. 1990, ApJ, 356, 62
Kellermann, K., & Owen, F. 1988, in Galactic and Extragalactic Radio Astronomy, ed. G. Verschuur & K. Kellermann (Berlin: Springer-Verlag), 563
Knapp, G., Bies, W., & van Gorkom, J. 1990, AJ, 99, 476
Knapp, G., Guhathakurta, P., Kim, D.-W., & Jura, M. 1989, ApJS, 70, 329
Knapp, G., & Patten, B. 1991, AJ, 101, 1609
Koski, A. 1978, ApJ, 223, 56
Kraemer, S., & Harrington, J. P. 1986, ApJ, 307, 478
Kuhr, H., Nauber, U., Pauliny-Toth, I., & Witzel, A. 1979, A Catalogue of Radio Sources (Bonn: Max-Planck-Institut fur Radioastronomie)
Laing, R., Riley, J., & Longair, M. 1983, MNRAS, 204, 151 (LRL)
Lawrence, A. 1991, MNRAS, 252, 586
Longair, M., & Seldner, M. 1979, MNRAS, 189, 433
Mazzarella, J., Graham, J., Sanders, D., & Djorgovski, S. 1993, ApJ, 409, 170
Miley, G. 1980, ARA&A, 18, 165
Miller, J. 1981, PASP, 93, 681
Mirabel, I. F., Sanders, D., & Kazes, I. 1989, ApJ, 340, L9
Morganti, R., Ulrich, M.-H., & Tadhunter, C. 1992, MNRAS, 254, 546
Netzer, H., & Laor, A. 1993, ApJ, 404, L51
Neugebauer, G., Miley, G., Soifer, B. T., & Clegg, P. 1986, ApJ, 308, 815
O'Dea, C. 1990a, in Compact Steep-Spectrum and GHz-Peaked Spectrum Radio Sources, ed. C. Fanti et al. (Bologna: Istituto di Radioastronomia), 182
———. 1990b, MNRAS, 245, 20P
O'Dea, C., Baum, S., & Stangellini, C. 1991, ApJ, 380, 66
Owen, F., & Laing, R. 1989, MNRAS, 238, 357 (OL)
Peacock, J., & Wall, J. 1982, MNRAS, 198, 843
Phinney, E. 1983, Ph.D. thesis, Cambridge Univ.
Pier, E., & Krolik, J. 1992, ApJ, 401, 99 (PK92)
———. 1993, ApJ, 418, 673 (PK93)
Prestage, L., & Peacock, J. 1988, MNRAS, 230, 131
Rees, M., Begelman, M., Blandford, R., & Phinney, E. 1982, Nature, 295, 17
Rowan-Robinson, M., & Crawford, J. 1989, MNRAS, 238, 523
Sanders, D., Phinney, E. S., Neugebauer, G., Soifer, B. T., & Matthews, K. 1989, ApJ, 347, 29
Scoville, N., Padin, S., Sanders, D., Soifer, B., & Yun, M. 1993, ApJ, 415, L75
Simkin, S. 1979, ApJ, 234, 56
Smith, E., & Heckman, T. 1989, ApJ, 341, 658
Smith, E., Heckman, T., & Illingworth, G. 1990, ApJ, 356, 399
Soifer, B. T., Houck, J., & Neugebauer, G. 1987, ARA&A, 25, 187
Spinrad, H., Djorgovski, S., Marr, J., & Aguilar, L. 1985, PASP, 97, 932
Stangellini, C., O'Dea, C., Baum, S., & Fanti, R. 1990, in Compact Steep-Spectrum and GHz Peaked Spectrum Radio Sources, ed. C. Fanti et al. (Bologna: Istituto di Radioastronomia), 17
Ulvestad, J. 1986, ApJ, 310, 136
Urry, C. M., Maraschi, L., & Phinney, S. 1991, Comm. Astrophys., 15, 111
Wise, M., O'Connell, R., Bregman, J., & Roberts, M. 1993, ApJ, 405, 94
Yates, M., & Longair, M. 1989, MNRAS, 241, 29
Zdziarski, A. 1986, ApJ, 305, 45
Zirbel, E., Baum, S., Heckman, T., & O'Dea, C. 1994, in preparation